

DTIC FILE COPY

# STRESS GAGE TESTING FOR WET CARES

1

AD-A232 178

June 1988

Final Report

By: S. A. Miller, D. D. Keough, and P. S. DeCarli

Prepared for:

U.S. Army Engineer  
WATERWAYS EXPERIMENT STATION  
P.O. Box 631  
Vicksburg, MS 39180-0631

Attention: Mr. Howard White

Contract No. DACA 39-86-K-0014

SRI Project PYU-2721

DTIC  
ELECTE  
MAR 15 1991  
S D

AD-A232 178  
Approved for public release  
Distribution Unlimited

SRI International  
333 Ravenswood Avenue  
Menlo Park, California 94025-3493  
(415) 326-6200  
TWX: 910-373-2046  
Telex: 334486



Q1 12 056

# REPORT DOCUMENTATION PAGE

1a REPORT SECURITY CLASSIFICATION UNCLASSIFIED			1b. RESTRICTIVE MARKINGS N/A since Unclassified	
2a SECURITY CLASSIFICATION AUTHORITY N/A since Unclassified			3 DISTRIBUTION/AVAILABILITY OF REPORT Approved for public release; distribution unlimited.	
2b DECLASSIFICATION/DOWNGRADING SCHEDULE N/A since Unclassified				
4 PERFORMING ORGANIZATION REPORT NUMBER(S) SRI Project PYU-2721			5. MONITORING ORGANIZATION REPORT NUMBER(S)	
5a NAME OF PERFORMING ORGANIZATION SRI International		6b OFFICE SYMBOL (If applicable)	7a. NAME OF MONITORING ORGANIZATION U.S. Army Engineer Waterways Experiment Station	
6c. ADDRESS (City, State, and ZIP Code) 333 Ravenswood Avenue Menlo Park, CA 94025-3493			7b. ADDRESS (City, State, and ZIP Code) P.O. Box 631 Vicksburg, MS 39180-0631	
8a. NAME OF FUNDING, SPONSORING ORGANIZATION U.S. Army Engineer Waterways Experiment Station		8b OFFICE SYMBOL (If applicable)	9 PROCUREMENT INSTRUMENT IDENTIFICATION NUMBER DACA39-86-K-0014	
9c ADDRESS (City, State, and ZIP Code) P.O. Box 631 Vicksburg, MS 39180-0631			10 SOURCE OF FUNDING NUMBERS	
			PROGRAM ELEMENT NO	PROJECT NO
			TASK NO	WORK UNIT ACCESSION NO
11 TITLE (Include Security Classification) STRESS GAGE TESTING FOR WET CARES				
12 PERSONAL AUTHOR(S) Miller, S. A., Keough, D. D., and DeCarli, P. S.				
13a TYPE OF REPORT Final		13b. TIME COVERED FROM 860926 TO 880702	14 DATE OF REPORT (Year, Month, Day) 880701	
15 PAGE COUNT				
16 SUPPLEMENTARY NOTATION				
17 COSATI CODES			18 SUBJECT TERMS (Continue on reverse if necessary and identify by block number)	
FIELD	GROUP	SUB-GROUP		
20	14		MIPV gage Gage validation Piezoresistance model	
20	11		Flatpack Rained sand Stress measurement	
			Groundshock measurement Particle velocity measurement	
19 ABSTRACT (Continue on reverse if necessary and identify by block number)				
<p>Groundshock measurements are important for interpreting field experiments and validating computer codes. However, the relationship between the measured gage output and free-field condition is not always direct. Therefore, it is necessary to validate groundshock measurements and determine how accurately the gage measurement represents the free-field condition. The main difficulty in gage validation is defining the free-field input to compare with the measurement without relying explicitly on material models of the free-field environment. In this report, we describe a material-independent approach to stress gage validation, and we apply this approach in two experiments using the mutual inductance particle velocity (MIPV) gage and the flatpack stress gage in rained sand test beds, a material of current interest to WES. The two experiments are (1) an MIPV gage validation experiment in a rained sand test bed performed in the SRI 2-foot-diameter flyer plate facility and (2) a flatpack stress gage validation experiment in a rained-sand test bed in the AFWL large-diameter flyer plate shot 8-4.</p>				
20 DISTRIBUTION/AVAILABILITY OF ABSTRACT <input checked="" type="checkbox"/> UNCLASSIFIED/UNLIMITED <input type="checkbox"/> SAME AS RPT <input type="checkbox"/> OTIC USERS			21 ABSTRACT SECURITY CLASSIFICATION UNCLASSIFIED	
22a NAME OF RESPONSIBLE INDIVIDUAL Mr. Howard White			22b TELEPHONE (Include Area Code) (601) 634-3391	22c OFFICE SYMBOL WESSE

## 19. ABSTRACT (Continued)

Another useful tool for meeting the validation objective is a computational model of flatpack response to interpret gage records and enhance the current empirical method for reducing flatpack data. To evaluate the current state of our computational flatpack response model and data reduction procedure, we (1) performed a gage calibration experiment with flatpacks and their components in a PMMA target and compared the observations with the results of a numerical simulation of the experiment using our computational flatpack response model and (2) applied the current transfer function approach to reducing flatpack data to the PMMA experiment.

The results of the validation efforts in rained sand test beds showed that (1) the MIPV gage measured the known particle velocity within the uncertainties of the experiment, +10%, -6% and (2) the flatpacks measured a peak free-field stress at the 20-cm test bed depth in the AFWL shot 8-4 at about 300 MPa, which is in good agreement with the known peak free-field stress at this depth determined from a Lagrangian analysis of (validated) particle velocity records.

The experimental and computational results of the PMMA experiment showed that (1) the flatpack response model reproduced the overall behavior of the flatpack, but the calculated gage output showed a larger gage signal than observed experimentally owing to inadequate piezoresistance coefficients for our ytterbium foils and (2) there is good agreement between the known and measured free-field stress using the transfer function approach to reducing flatpack data.

On the basis of the results of this work, we recommend (1) applying the gage validation approach to other materials (e.g., wet soils, hard rock); (2) increasing the diameter of the AFWL flyer plate facility for rained sand test beds and measuring the time of arrival and magnitude of two-dimensional effects in subsequent experiments, (3) performing high resolution two-dimensional calculations of flatpack response to more accurately determine the mechanical state of the ytterbium foil inside the flatpack, and (4) continuing testing of our ytterbium foils to refine the piezoresistance coefficients used to model ytterbium in our flatpack response model.

Accession for	
NTIS GRA&I	✓
DTIC TAB	
Unannounced	
Justification	
By	
D. F. Gibson	
Date	
Dist	
A-11	

# Conversion factors for U.S. Customary to metric (SI) units of measurement

MULTIPLY  $\longrightarrow$  BY  $\longrightarrow$  TO GET  
TO GET  $\longleftarrow$  BY  $\longleftarrow$  DIVIDE

angstrom	1.000 000 X E -10	meters (m)
atmosphere (normal)	1.013 25 X E +2	kilo pascal (kPa)
bar	1.000 000 X E +2	kilo pascal (kPa)
barn	1.000 000 X E -28	meter <sup>2</sup> (m <sup>2</sup> )
British thermal unit (thermochemical)	1.054 350 X E +3	joule (J)
calorie (thermochemical)	4.184 000	joule (J)
cal (thermochemical)/cm <sup>2</sup>	4.184 000 X E -2	mega joule/m <sup>2</sup> (MJ/m <sup>2</sup> )
curie	3.700 000 X E +1	*giga becquerel (GBq)
degree (angle)	1.745 329 X E -2	radian (rad)
degree Fahrenheit	$t_F = (t_C + 459.67)/1.8$	degree kelvin (K)
electron volt	1.602 19 X E -19	joule (J)
erg	1.000 000 X E -7	joule (J)
erg/second	1.000 000 X E -7	watt (W)
foot	3.048 000 X E -1	meter (m)
foot-pound-force	1.355 818	joule (J)
gallon (U. S. liquid)	3.785 412 X E -3	meter <sup>3</sup> (m <sup>3</sup> )
inch	2.540 000 X E -2	meter (m)
jerk	1.000 000 X E +9	joule (J)
joule/kilogram (J/kg) (radiation dose absorbed)	1.000 000	Gray (Gy)
kilotons	4.183	terajoules
kip (1000 lbf)	4.448 222 X E +3	newton (N)
kip/inch <sup>2</sup> (ksi)	6.894 757 X E +3	kilo pascal (kPa)
ktap	1.000 000 X E +2	newton-second/m <sup>2</sup> (N-s/m <sup>2</sup> )
micron	1.000 000 X E -6	meter (m)
mil	2.540 000 X E -5	meter (m)
mile (international)	1.609 344 X E +3	meter (m)
ounce	2.834 952 X E -2	kilogram (kg)
pound-force (lbs avoirdupois)	4.448 222	newton (N)
pound-force inch	1.129 848 X E -1	newton-meter (N-m)
pound-force/inch	1.751 268 X E +2	newton/meter (N/m)
pound-force/foot <sup>2</sup>	4.788 026 X E -2	kilo pascal (kPa)
pound-force/inch <sup>2</sup> (psi)	6.894 757	kilo pascal (kPa)
pound-mass (lbm avoirdupois)	4.535 924 X E -1	kilogram (kg)
pound-mass-foot <sup>2</sup> (moment of inertia)	4.214 011 X E -2	kilogram-meter <sup>2</sup> (kg-m <sup>2</sup> )
pound-mass/foot <sup>3</sup>	1.601 846 X E +1	kilogram/meter <sup>3</sup> (kg/m <sup>3</sup> )
rad (radiation dose absorbed)	1.000 000 X E -2	**Gray (Gy)
roentgen	2.579 760 X E -4	coulomb/kilogram (C/kg)
shake	1.000 000 X E -8	second (s)
slug	1.459 390 X E +1	kilogram (kg)
torr (mm Hg, 0° C)	1.333 22 X E -1	kilo pascal (kPa)

\*The becquerel (Bq) is the SI unit of radioactivity; 1 Bq = 1 event/s.

\*\*The Gray (Gy) is the SI unit of absorbed radiation.

A more complete listing of conversions may be found in "Metric Practice Guide E 380-74," American Society for Testing and Materials

# TABLE OF CONTENTS

<u>Section</u>	<u>Page</u>
CONVERSION TABLE .....	iii
LIST OF ILLUSTRATIONS .....	v
1 INTRODUCTION AND SUMMARY .....	1-1
1.1 Method for Particle Velocity and Stress Gage Validation .....	1-1
1.2 Computational Flatpack Response Model and Data Reduction .....	1-3
1.3 MIPV Gage Validation .....	1-3
1.4 AFWL Flyer Plate Shot 8-4 .....	1-4
1.5 Computational Flatpack Response Model .....	1-5
1.6 Recommendations .....	1-6
2 MIPV GAGE VALIDATION EXPERIMENT .....	2-1
2.1 Gage Operation .....	2-1
2.2 Experimental Configuration .....	2-2
2.3 Free-Field Particle Velocity .....	2-10
3 LARGE DIAMETER FLYER PLATE SHOT 8-4 .....	3-1
3.1 Experimental Configuration .....	3-1
3.2 Experimental Results .....	3-6
3.3 Free-Field Stress from Lagrange Analysis .....	3-6
3.4 Comparison of Known and Measured Free-Field Stress .....	3-10
4 COMPUTATIONAL MODEL OF FLATPACK RESPONSE AND DATA REDUCTION PROCEDURES .....	4-1
4.1 Experimental Configuration .....	4-1
4.2 Experimental Results .....	4-1
4.3 Results of Calculating the PMMA Experiment .....	4-5
4.3.1 Computational Model .....	4-5
4.3.2 Transfer Function for Reducing Flatpack Data .....	4-9
5 RECOMMENDATIONS FOR FUTURE WORK .....	5-1
6 REFERENCES .....	6-1

# LIST OF ILLUSTRATIONS

<u>Figure</u>		<u>Page</u>
1.1	Method for stress gage validation .....	1-2
2.1	Two-foot-diameter flyer plate facility .....	2-3
2.2	Side view of experimental configuration of MIPV gage validation experiment in dry sand test bed .....	2-4
2.3	Front view of instrumented target for MIPV gage validation experiment in dry sand test bed .....	2-5
2.4	Side view of wave-resolving TOA pins for shock velocity measurement in MIPV gage validation experiment in dry sand .....	2-6
2.5	MIPV gage in Plexiglas casket used in gage validation experiment in dry sand .....	2-8
2.6	Back view of target before raining sand, showing MIPV gages in caskets and TOA pins .....	2-8
2.7	Back view of target after raining sand test bed .....	2-9
2.8	Front view of completed sand target .....	2-9
2.9	Pressure-particle velocity diagram for defining bounds on particle velocity .....	2-11
2.10	MIPV gage records in dry sand test bed .....	2-12
3.1	SRI instrumentation layout in AFWL large flyer plate shot 8-4 .....	3-2
3.2	Ytterbium element in PMMA block used for TOA/peak stress measurement in rained sand test bed shot 8-4 .....	3-4
3.3	Schematic of flatpack stress gage used in large flyer plate shot 8-4 .....	3-5
3.4	MIPV gage in PMMA casket used in dry sand test bed shot 8-4 .....	3-7
3.5	Side view of instrumentation layout in rained sand test bed shot 8-4 .....	3-8
3.6	MIPV gage records obtained from 8-foot (2.4-m) flyer plate shot 8-4 .....	3-9
3.7	Early-time stress history computed from Lagrange analysis at 20-cm depth in sand test bed for 8-foot (2.4-m) flyer plate shot 8-4 .....	3-11
3.8	Comparison of flatpack gage stress histories with free-field stress history calculated from Lagrange analysis .....	3-12

# LIST OF ILLUSTRATIONS (Continued)

<u>Figure</u>		<u>Page</u>
3.9	Comparison of flatpack stress histories using filter function and calculated stress history from Lagrange analysis .....	3-13
3.10	Comparison of AFWL EOS with Skidmore EOS and SRI data .....	3-15
4.1	Configuration for 24-inch (60.9-cm) gas gun calibration experiment in PMMA showing two field flatpacks .....	4-2
4.2	Front view of layout in gage calibration experiment .....	4-3
4.3	Composite relative resistance change records for encapsulated gages (B1-B5) obtained from gage calibration experiment in PMMA .....	4-4
4.4	Relative resistance change records for flatpack stress gages in gage calibration experiment .....	4-6
4.5	Comparison of relative resistance change records for flatpack stress gage and ytterbium element in Kapton/adhesive encapsulant ....	4-7
4.6	Comparison of relative resistance change records for flatpack stress gage and ytterbium elements in Teflon/epoxy encapsulant .....	4-8
4.7	Calculated relative resistance change for flatpack and encapsulated ytterbium element using electro-mechanical piezoresistance (EP) model .....	4-10
4.8	Empirical flatpack unfolding function for data reduction .....	4-11
4.9	Composite stress histories reduced from $\Delta R/R_0$ records for encapsulated elements (B1-B5) in gage calibration experiment .....	4-13
4.10	Comparison of stress history reduced from relative resistance change record for photo-etched ytterbium element in Kapton/adhesive encapsulant .....	4-14
4.11	Comparison of stress histories reduced from relative resistance change records for flatpack stress gage and ytterbium elements in Teflon/epoxy encapsulant .....	4-15
4.12	Load/unload path of ytterbium element inside a flatpack calculated using flatpack response model .....	4-17

## SECTION 1

### INTRODUCTION AND SUMMARY

This work was initiated to validate ground shock measurements in wet soils; however, during the program, the material emphasis changed from wet to dry soils, and results of this study reflect that change.

Measurement of physical quantities in laboratory and field experiments is vital for interpreting experimental results and for validating computer code calculations. In particular, ground shock particle velocity and stress measurements are important in ground motion and structures programs. However, the relationship between the gage output and the actual free-field quantity being measured is not always direct. Therefore, it is necessary to validate the measurements and determine how accurately the gage output represents the free-field input.

Our objectives were to (1) validate measurements of two types of gages, the mutual inductance particle velocity (MIPV) gage and the flatpack stress gage, in a material of current interest and (2) develop and test parameters for our computational model of flatpack response to interpret the gage output and enhance the data reduction procedure.

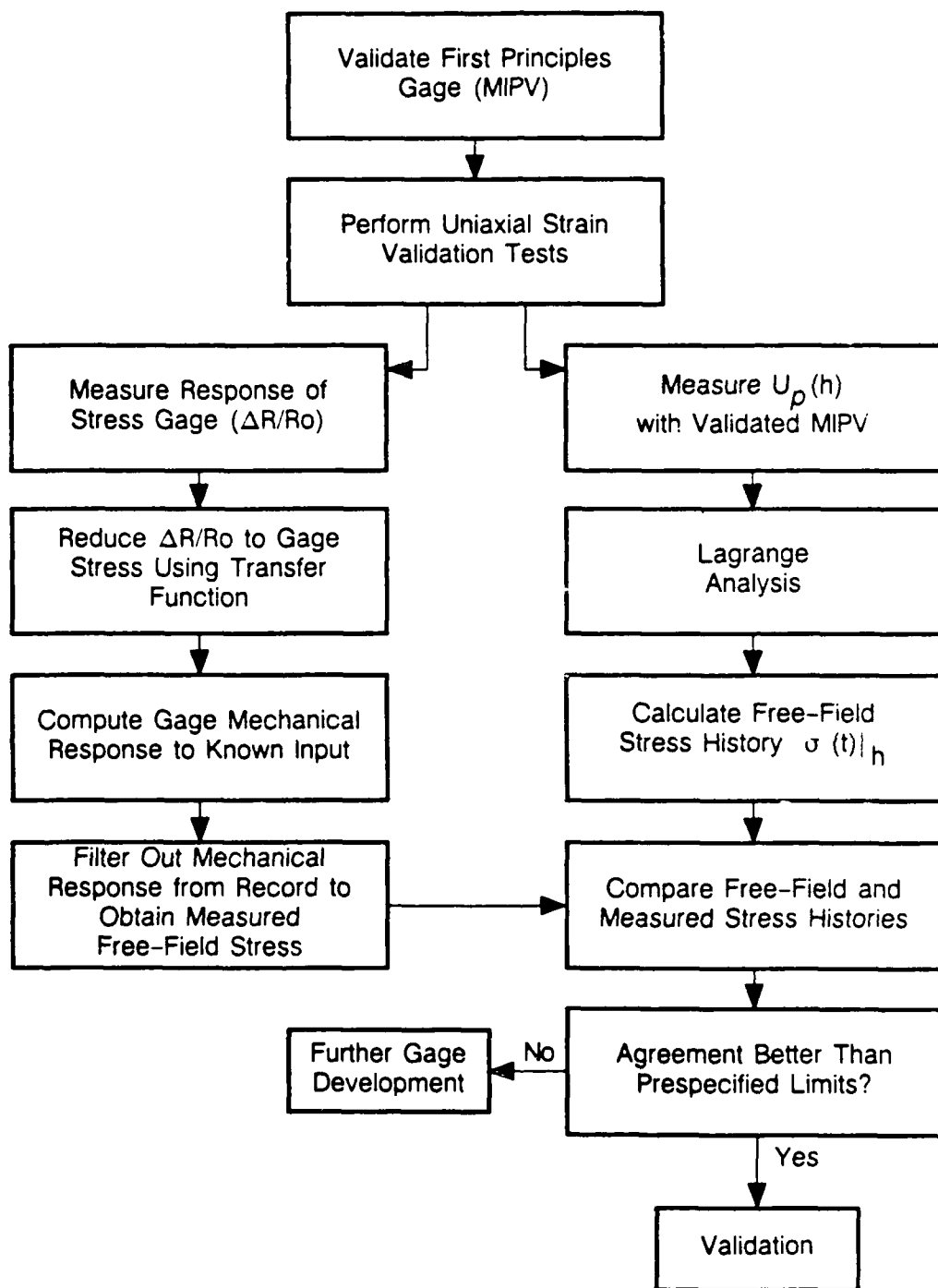
The main difficulty in validating measurements is defining the free-field input without relying explicitly on (sometimes inadequate) material models of the free-field environment. In this report, we present a material-independent approach to MIPV and stress gage validation, and we apply this approach to dry sand test beds.

Our approach to developing the computational flatpack response model was to (1) measure piezoresistance coefficients for our ytterbium foil, (2) perform a 2-foot-diameter flyer plate experiment with a PMMA (polymethyl metacrylate) target containing flatpacks and their components to generate flatpack response data to a well-defined input, and (3) evaluate the flatpack response model by comparing a computational simulation of the PMMA experiment with the experimental data.

#### 1.1 METHOD FOR PARTICLE VELOCITY AND STRESS GAGE VALIDATION.

The material-independent approach to stress gage validation is summarized in the flow chart shown in Figure 1.1. The first step is to validate a gage where the signal is directly related to free-field input from a first principles relationship. One such gage is the mutual inductance particle velocity (MIPV) gage, whose operating principle is derived directly from Maxwell's equations. The SRI 2-foot gas gun





RA-2721-1

Figure 1.1. Method for stress gage validation.

is a useful facility for validating the MIPV gage, because it provides a well-defined, long-duration uniaxial strain flow field while maintaining the quality control environment of the laboratory. Once the MIPV gage is validated, the gage can be used in other uniaxial strain validation tests such as the SRI compact reusable airblast simulator (CRABS) and the AFWL large-diameter flyer plate facility.

Validating stress gage measurements is a parallel process of defining the free-field input and measuring the gage output. Defining the free-field input involves measuring particle velocity (with the validated MIPV gage) at different depths in the test bed and performing a Lagrangian analysis to calculate the free-field stress history, in particular, at the test bed depths of the flatpack stress gages. Concurrently, the measured relative resistance change ( $\Delta R/R_0$ ) output of the gage is reduced to stress through transfer functions that relate resistance change to stress and separate the gage response to the free-field stress from the mechanical response of the gage package.

Validation of the stress measurement depends on the comparison of the known free-field input stress with the measured stress. If the agreement is better than prespecified limits, then the gage is validated in that test bed material. If the agreement is less than specified, further gage development is necessary.

## 1.2 COMPUTATIONAL FLATPACK RESPONSE MODEL AND DATA REDUCTION.

Current methods for reducing flatpack data use empirical transfer functions to relate the gage output ( $\Delta R/R_0$ ) to stress. A more rigorous approach to interpreting flatpack data is to use a computational model of flatpack response based on an electromechanical piezoresistance (EP) model for the ytterbium and known material models of the flatpack components (i.e., steel and insulator). Our objectives were to (1) evaluate the current state of the EP model by comparing observed and calculated output of a well-controlled calibration experiment of a flatpack in PMMA and (2) evaluate the transfer function approach to reducing flatpack data.

## 1.3 MIPV GAGE VALIDATION.

The results of the 2-foot gas gun MIPV gage validation experiment in a dry, rained sand test bed demonstrated that the gage measured the known input particle velocity within the uncertainties of the experiment (+10%, -6%). Because the gages were validated in self-contained modules (or caskets), the validation can be extended to field use where the module approach to gage emplacement is used.

Caskets are particularly useful for rained sand test beds because they provide uniform density around the gage and ensure intimate contact between the active gage area and the test material.

#### 1.4 AFWL FLYER PLATE SHOT 8-4.

Our instrumentation effort in the AFWL 8-foot-diameter flyer plate shot 8-4 showed (1) a peak free-field stress at the 20-cm depth in the sand test bed of about 300 MPa calculated from a Lagrangian analysis of the validated MIPV records and (2) a measured peak free-field stress from the flatpack stress gages of about 300 MPa but consistent 5% to 30% underregistration of the known free-field stress following the peak.

The measured peak stress of 300 MPa was significantly lower than the peak determined by other investigators, and the differences are still a subject of debate. They may be due to the sand material model used by AFWL to interpret TOA and strain can measurements in the test bed. Because the AFWL approach to determining the test bed stress relies explicitly on a material model for the test bed, we believe that the more rigorous, first principles approach is required for validation studies. The underregistration of the measured free-field stress following the peak is not yet understood but may be due to (unquantified) two-dimensional effects from the edge of the test bed.

#### 1.5 COMPUTATIONAL FLATPACK RESPONSE MODEL.

The computational simulation of the PMMA calibration experiment using the flatpack response model with laboratory determined piezoresistance coefficients showed a good correlation between the calculated and observed features of flatpack response, namely, (1) an initial overshoot of the free-field stress and subsequent oscillatory response of the flatpack during the equilibration of the gage package with free-field stress and (2) a larger equilibrium relative resistance change level for flatpack gages than for gages in encapsulant only at the same free-field stress. Although the overall flatpack response was modeled, the calculated relative resistance change levels were about 30%-40% higher than observed experimentally, indicating that the piezoresistance coefficients determined from laboratory uniaxial tension tests need further refinement.

The results of the empirical (calibration curve) transfer function approach to reducing resistance change records to stress showed excellent agreement between the measured and the known free-field stress in the PMMA gage calibration experiment,

and this method for reducing flatpack data is supported by the load/unload behavior of the calculated flatpack response.

#### 1.6 RECOMMENDATIONS.

On the basis of the results of this work, we recommend (1) applying the gage validation approach to other materials (e.g., wet soils, hard rock), (2) increasing the diameter of the AFWL flyer plate facility for rained sand test beds and measuring the time of arrival and magnitude of two-dimensional effects in subsequent experiments, (3) performing high resolution two-dimensional calculations of flatpack response to more accurately determine the mechanical state of the ytterbium foil inside the flatpack, and (4) continuing testing of our ytterbium foils to refine the piezoresistance coefficients used to model ytterbium on flatpack response model.

## SECTION 2

### MIPV GAGE VALIDATION EXPERIMENT

We performed a uniaxial strain plate impact experiment using a dry, rained sand test bed in the SRI 2-foot gas gun facility. Our objectives were to (1) determine how accurately the MIPV gage measures the known particle velocity in a well-controlled uniaxial strain environment, (2) validate the MIPV gage using a gage emplacement technique adaptable to field use, and (3) evaluate MIPV gages constructed of different wire types and reinforcement techniques to determine survivability and overall performance of the different designs.

The approach was to generate a known free-field particle velocity history in a dry sand test bed and compare the known to measured particle velocities. We used self-contained modules (or caskets) to emplace the MIPV gages because this technique allows quality control of the test environment around the gage and is easily adaptable to field conditions.

#### 2.1 GAGE OPERATION.

The mutual-inductance particle velocity gage has been extensively developed for use in a low stress (0 to 2 GPa) environment.<sup>1-3</sup> The gage consists of closely wound primary and secondary windings embedded in the test matrix material. The primary winding is excited with a constant current before arrival of the stress wave, linking the primary and secondary (or signal) windings through the magnetic flux. Upon arrival of the stress wave, the front of the gage moves with the matrix material at the local particle velocity. As the front of the gage moves, the length of the gage changes and generates an emf in the signal loop. The recorded signal voltage (E) is related to the particle velocity from the relation

$$E = MI/Lu$$

where M is the mutual inductance linking the primary and secondary loops, L is the initial gage length, and u is the particle velocity. The gage is operational until the shock wave reaches the back end of the gage.

Although the gage principle is well established, gage validation has been relatively limited, with validation efforts in materials with known shock characteristics like PMMA and fused silica.<sup>2,3</sup> Before this work, the MIPV gage had not been validated in the current material of interest, namely, dry sand.

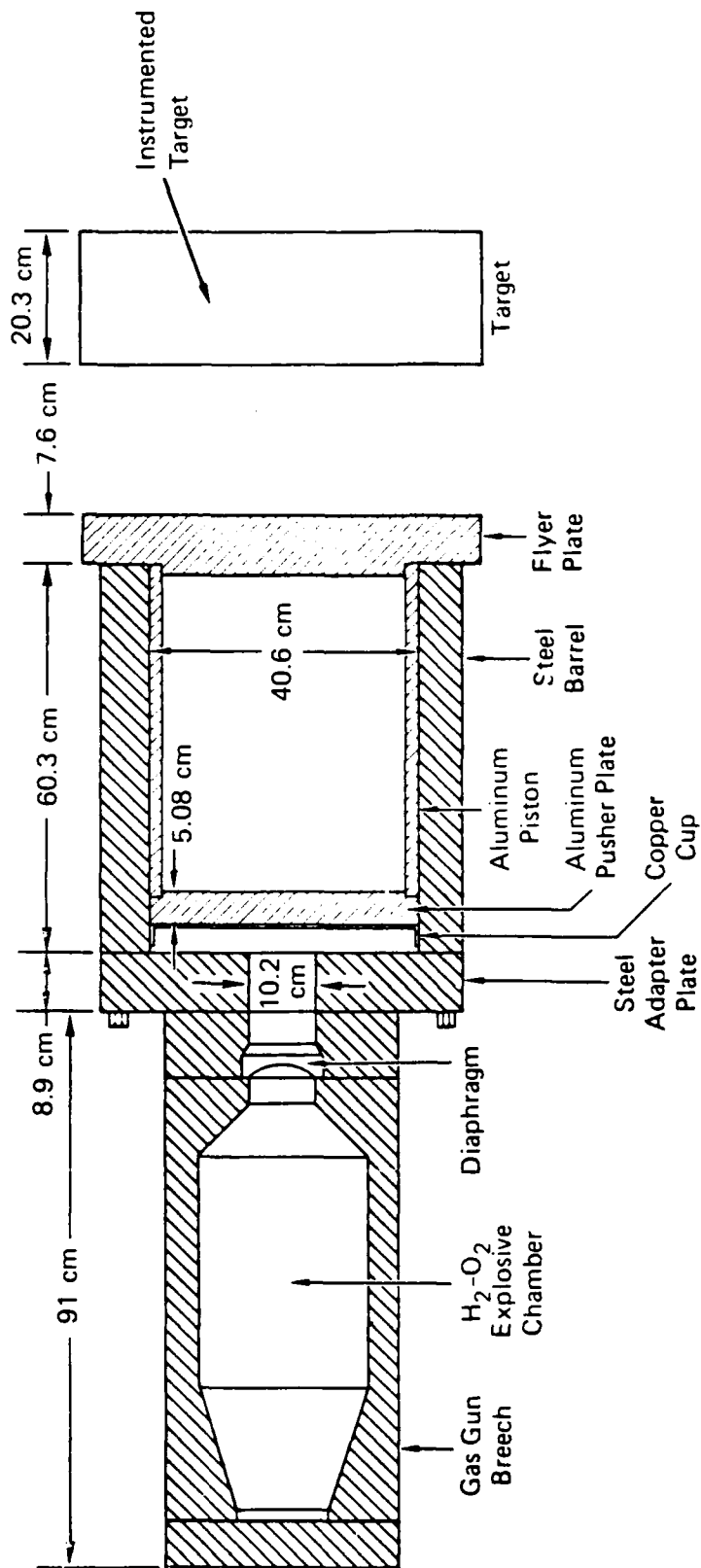
## 2.2 EXPERIMENTAL CONFIGURATION.

We performed the MIPV gage validation experiment in our 2-foot gas gun shown schematically in Figure 2.1. In this facility, a hydrogen-oxygen mixture is detonated in an explosive chamber, accelerating a 2-foot-diameter flyer plate. The flyer plate impacts the target in a vacuum chamber at velocities ranging from 50-100 m/s, generating a shock pressure in the target from 0.5 to 5 kbar (50 to 500 MPa), depending on the flyer plate and target materials. The large flyer plate and target diameters allow for a long-duration (50-100  $\mu$ s) uniaxial strain environment.

The side view of the MIPV gage validation experiment is shown in Figure 2.2. In this plate impact experiment, a PMMA flyer plate impacted a PMMA cover plate at  $87 \pm 2$  m/s, generating a stress wave (square wave pulse) into the sand test bed. The flyer plate was supported by low-density honeycomb and an aluminum plate that prohibited acceleration-induced deflections while providing a free surface at the rear of the flyer plate. The target consisted of a 1.9-cm cover plate attached to an aluminum ring and backed by a rained sand test bed. The sand was contained by an aluminum plate connected at the back of the target, and a hole at the top of the target provided an outlet for the escape of air in the sand voids during the vacuum pumping process. Test bed instrumentation included stress-wave resolving time-of-arrival (TOA) rods for shock velocity measurement and four MIPV gages in Plexiglas caskets. The instrumentation is shown in the front view of the target in Figure 2.3.

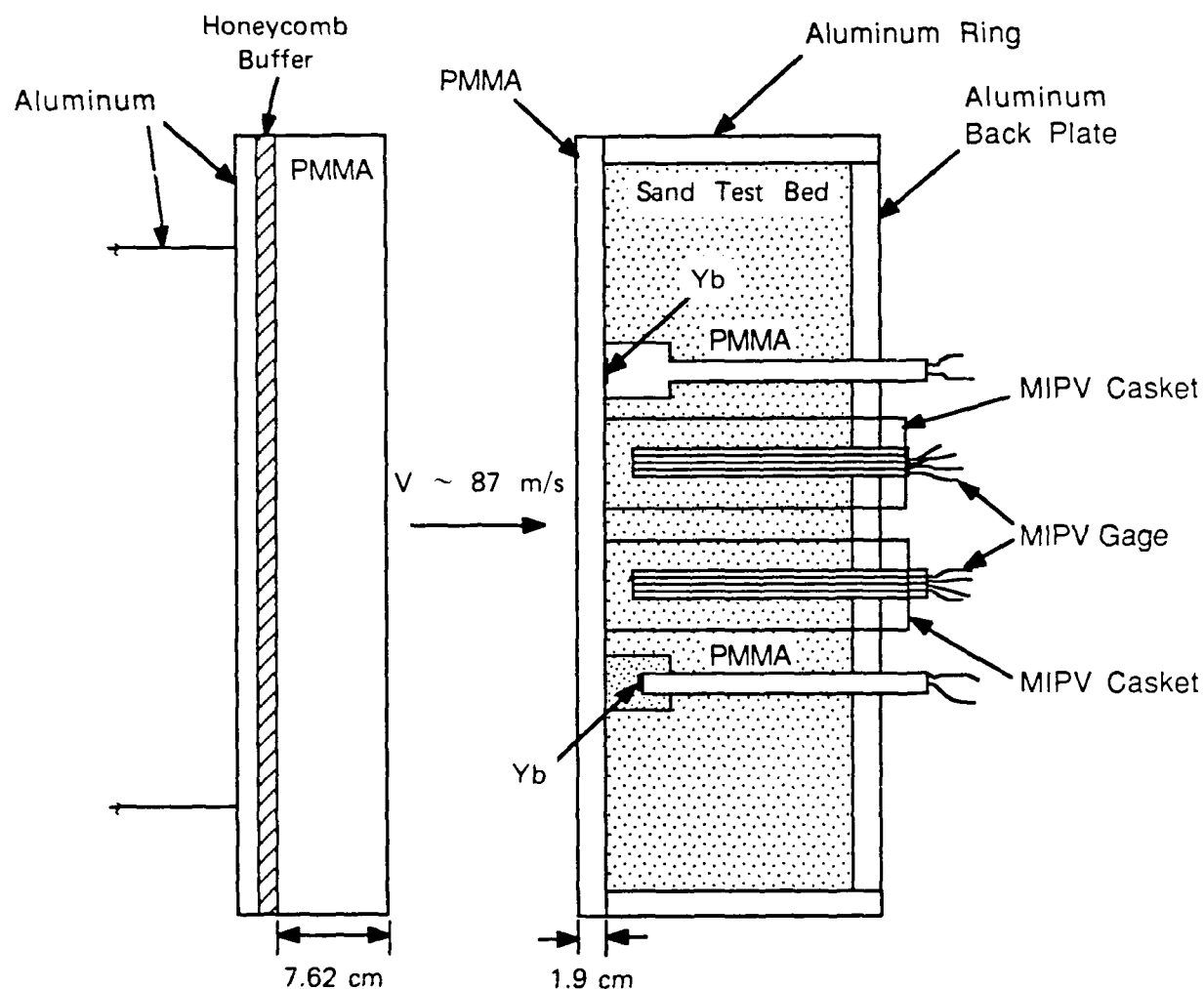
As discussed in Section 2.3, shock velocity measurement is needed to define the free-field particle velocity history; in this experiment, we used ytterbium-sensing elements at different depths in the target to (1) measure the shock velocity and (2) resolve the waveform as it propagated through the sand test bed. The TOA rods are shown schematically in Figure 2.4. A vapor-deposited ytterbium element was placed at the front end of a Plexiglas rod, protected from the sand by a very thin (0.08-cm) Plexiglas disk. We rained sand into the region above the ytterbium element and closed the container with another 0.08-cm Plexiglas disk. During target construction, the TOA rods were mounted to the rear surface of the target cover plate before raining the sand test bed. The depth of the sand ( $d$ ) ranged from 0 (to measure the input wave from the PMMA symmetric impact) to 1.27 cm.

The main problem with using MIPV gages in rained sand test beds is that the active part of the gage (the front surface) shadows the raining of the sand, thereby allowing either a gap directly behind the front surface, or at best, a lower sand density. If a gap forms behind the gage, the active gage region initially moves at



JA-6917-1A

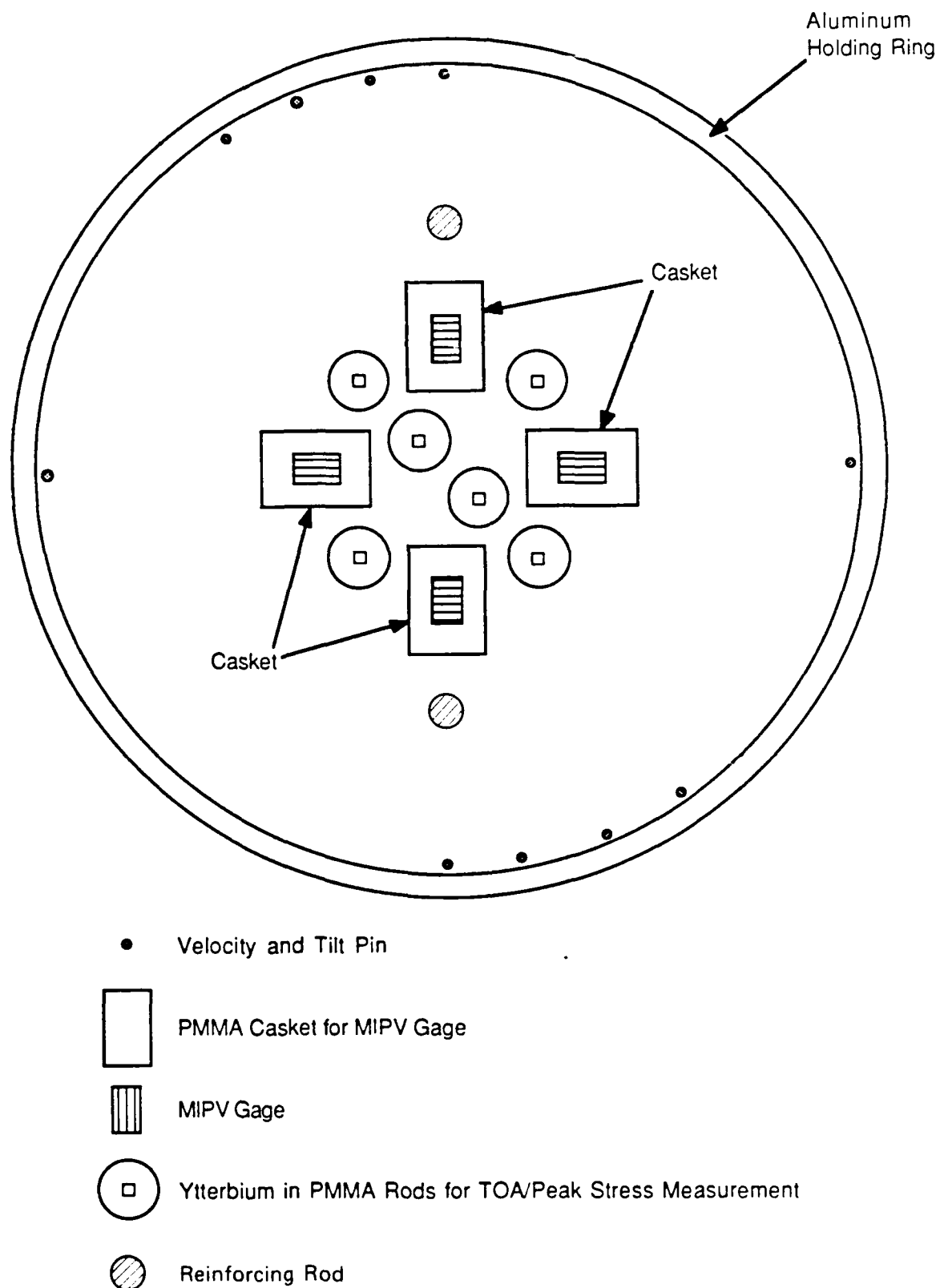
Figure 2.1. Two-foot-diameter flyer plate facility.



RA-M-314543-9

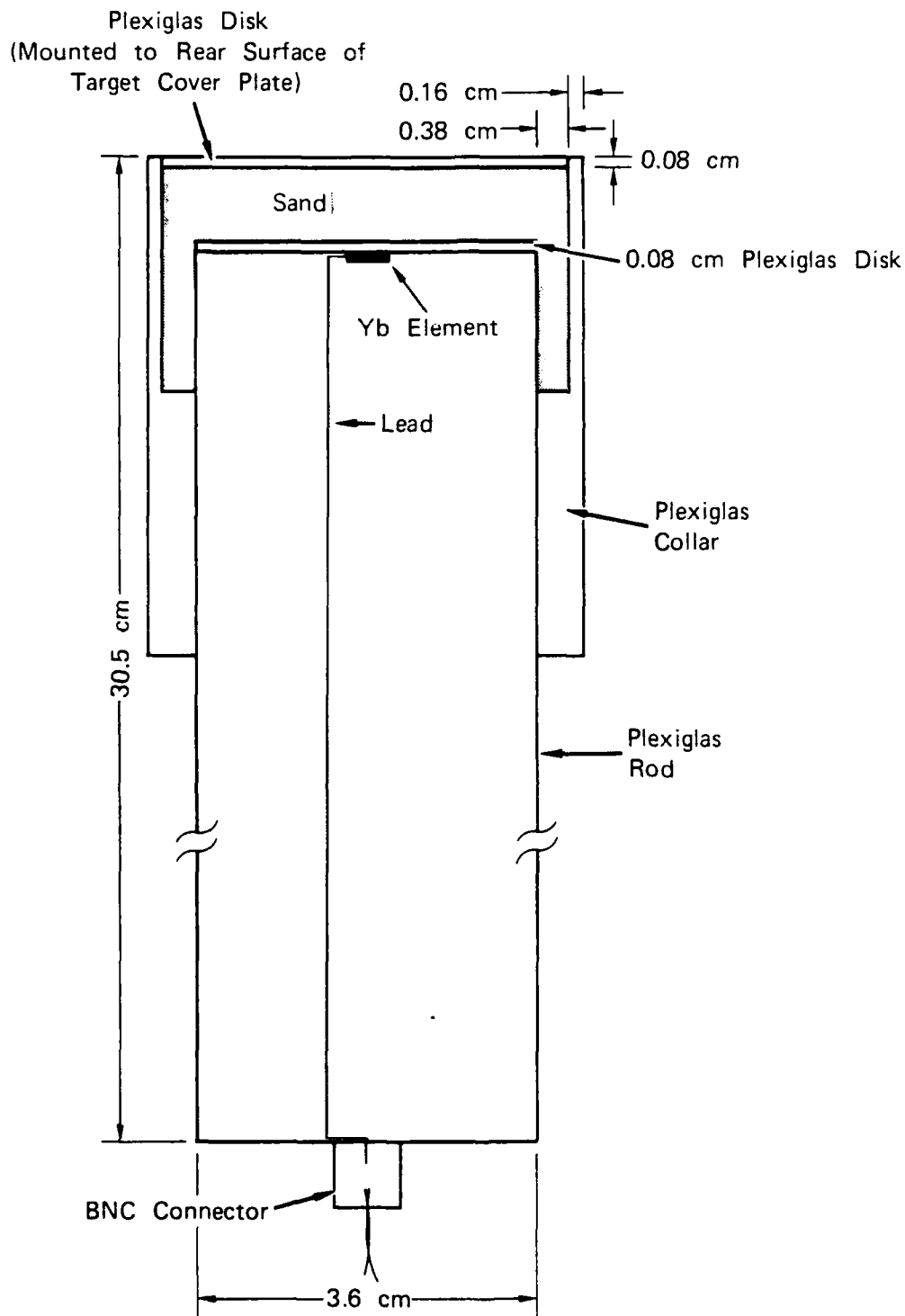
Figure 2.2. Side view of experimental configuration of MIPV gage validation experiment in dry sand test bed.





RA-M-314543-8A

Figure 2.3. Front view of instrumented target for MIPV gage validation experiment in dry sand test bed.



RA-2721-2

Figure 2.4. Side view of wave-resolving TOA pins for shock velocity measurement in MIPV gage validation experiment in dry sand.

the free surface velocity and not sand particle velocity. An alternative approach for emplacing MIPV gages in rained sand test beds is to use self-contained modules, or caskets, to produce a uniform density around the gage and ensure intimate contact of the test material with the active gage region. This technique is readily adaptable to field use.

A typical MIPV gage in a Plexiglas casket for this experiment is shown in Figure 2.5. The procedure is to rain the test material from a height of 1.2 m, perpendicular to the wave propagation direction, seal the module, and place the completed gage package into the test bed. The gage package is then supported in the test bed by subsequent raining around the gage package. Using this technique insures uniform density around the gage and intimate contact of the gage and sand test bed. The front edge of the MIPV gage was nominally 1.13 cm from the rear surface of the PMMA target cover plate.

We investigated MIPV gages of the same geometric design, but we varied the materials used to make the gage to determine the importance of differences in gage construction. Three different MIPV gage types were investigated: (1) solid wire, (2) stranded wire, and (3) stranded wire with fiberglass reinforcement. The advantage of stranded over solid wire gages is that they are relatively weak in the direction of the flow, whereas solid wire gages may, at low velocities, restrict the flow with the surrounding material because of rigidity of the gage leads. We tested a stranded wire gage reinforced with fiberglass because at higher particle velocities, gage survival becomes important.

We rained the sand from the back of the target to prevent disturbing the measurement region of the test bed when striking off the extra sand at the end of the raining process. The procedure was to (1) rain sand and seal the TOA measurement rods and MIPV gage caskets and measure the density, (2) attach the rods and caskets to the rear surface of the PMMA cover plate using a plastic welding compound, (3) rain the remainder of the test bed from the back of the target, (4) strike off the extra sand, and (5) attach the aluminum plate to the aluminum ring at the target rear surface. A back view of the target showing the TOA and MIPV gages in caskets before raining the surrounding test bed is shown in Figure 2.6. The back view of the test bed after raining the sand is shown in Figure 2.7, and a front view of the completed target is shown in Figure 2.8. The two Plexiglas rods seen at the top and bottom of the target are reinforcing rods to restrict cover plate deflections from the static sand load.

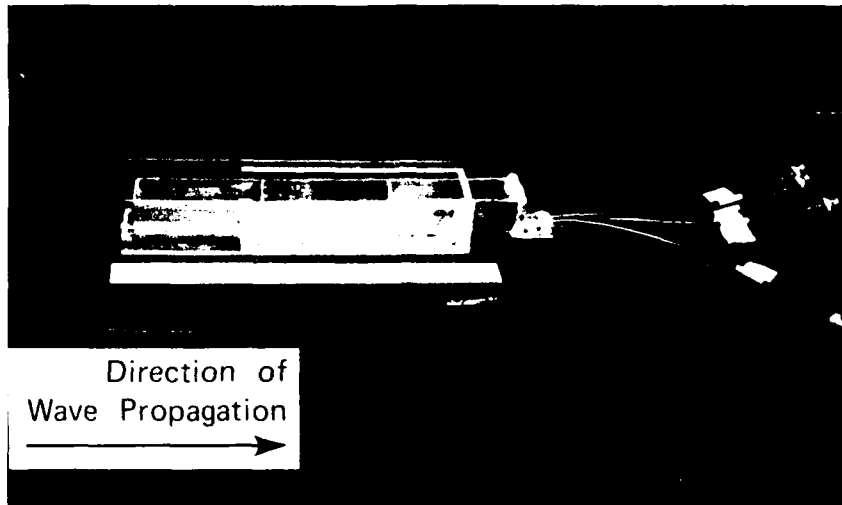


Figure 2.5. MIPV gage in Plexiglas casket used in gage validation experiment in dry sand. Scale is 30.5 cm.

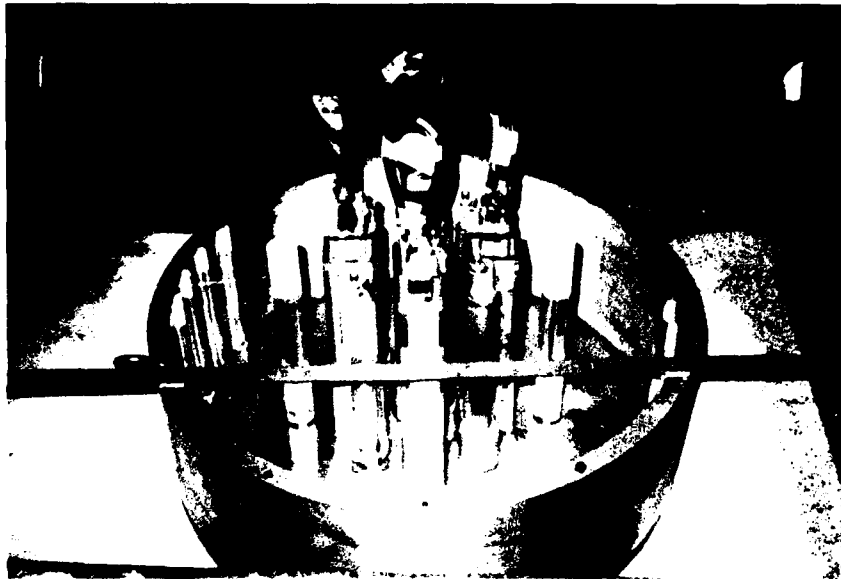


Figure 2.6. Back view of target before raining sand, showing MIPV gages in caskets and TOA pins. Scale is 100 cm.

RP-2721-3

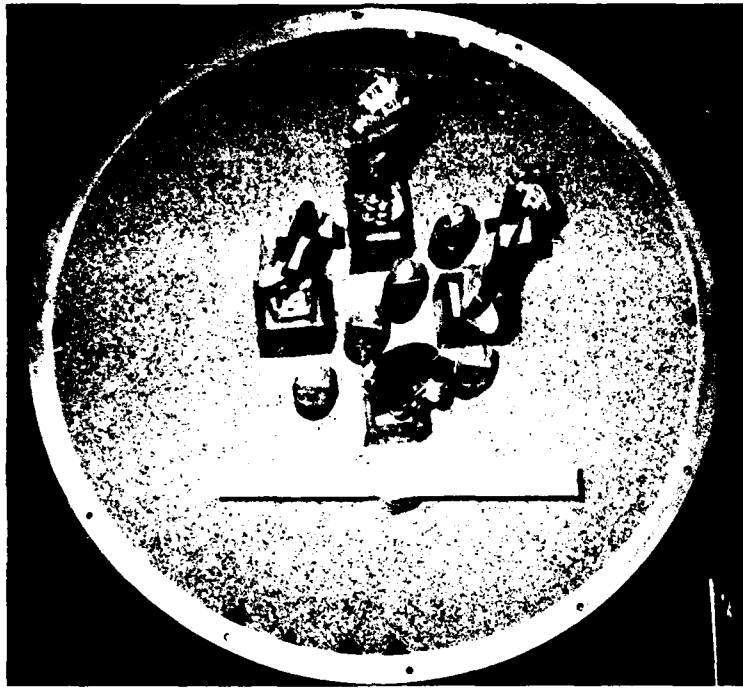


Figure 2.7. Back view of target after raining sand test bed. Scale is 30.5 cm.



Figure 2.8. Front view of completed sand target. Scale is 45.7 cm.

RP-2721-4

The test bed material was dry Monterey sand, which is predominantly  $\text{SiO}_2$ . We approximated the grain size distribution of the sand used in the test bed for the AFWL large flyer plate calibration facility, and we measured a rained density of  $1.72 \pm 0.02 \text{ g/cm}^3$ .

### 2.3 FREE-FIELD PARTICLE VELOCITY.

The free-field particle velocity in the sand test bed was determined using the well-known impedance mismatch technique. For a symmetric impact (same flyer and target material) of a well-characterized material, the particle velocity is defined by measuring the shock impedance ( $Z = \rho_0 U_s$ , where  $\rho_0$  is initial density and  $U_s$  is the shock velocity) of the sand and the impact velocity of the projectile. The particle velocity in the sand is determined from the intersection of the impedance (or Rayleigh) line with the known Hugoniot of PMMA. This determination of the particle velocity is shown in the pressure-particle plane in Figure 2.9. Upon impact of the PMMA flyer with the target cover plate, the pressure and particle velocity amplitude in the target and flyer are defined by the intersection of the left-going (flyer plate) and right-going (target cover plate) PMMA Hugoniot. When the wave reaches the PMMA/sand interface, the lower impedance of the sand causes a decrease in stress and an increase in particle velocity of the propagated pulse. The pressure and particle velocity amplitude of the propagated pulse is defined by intersection of the Rayleigh line and the PMMA Hugoniot. In this experiment, the initial density is known and we measured the shock velocity.

Because of a long rise time observed in the sand, we could not unambiguously determine the shock velocity. Nevertheless, we can place bounds on this measurement from the minimum and maximum measured shock velocity, and in this experiment, the measured shock velocity ranged from 0.63 to 0.86 mm/ $\mu\text{sec}$ . The experimental uncertainties of impact velocity, shock velocity, and initial density are shown as the shaded region in Figure 2.9. After experimental uncertainties are accounted for, the range of sand particle velocity in the test bed is bounded by a minimum of 58 m/s and a maximum of 68 m/s.

The measured particle velocity histories for the four MIPV gages are shown in Figure 2.10, and the known particle velocity range (58 to 68 m/s) is shown as the shaded region in that figure. All MIPV gages registered a constant peak particle velocity of  $62 \pm 2 \text{ m/s}$  and a scatter of about 3%, and all fell within the experimental uncertainties of about +10% -6% of the average measured velocity.

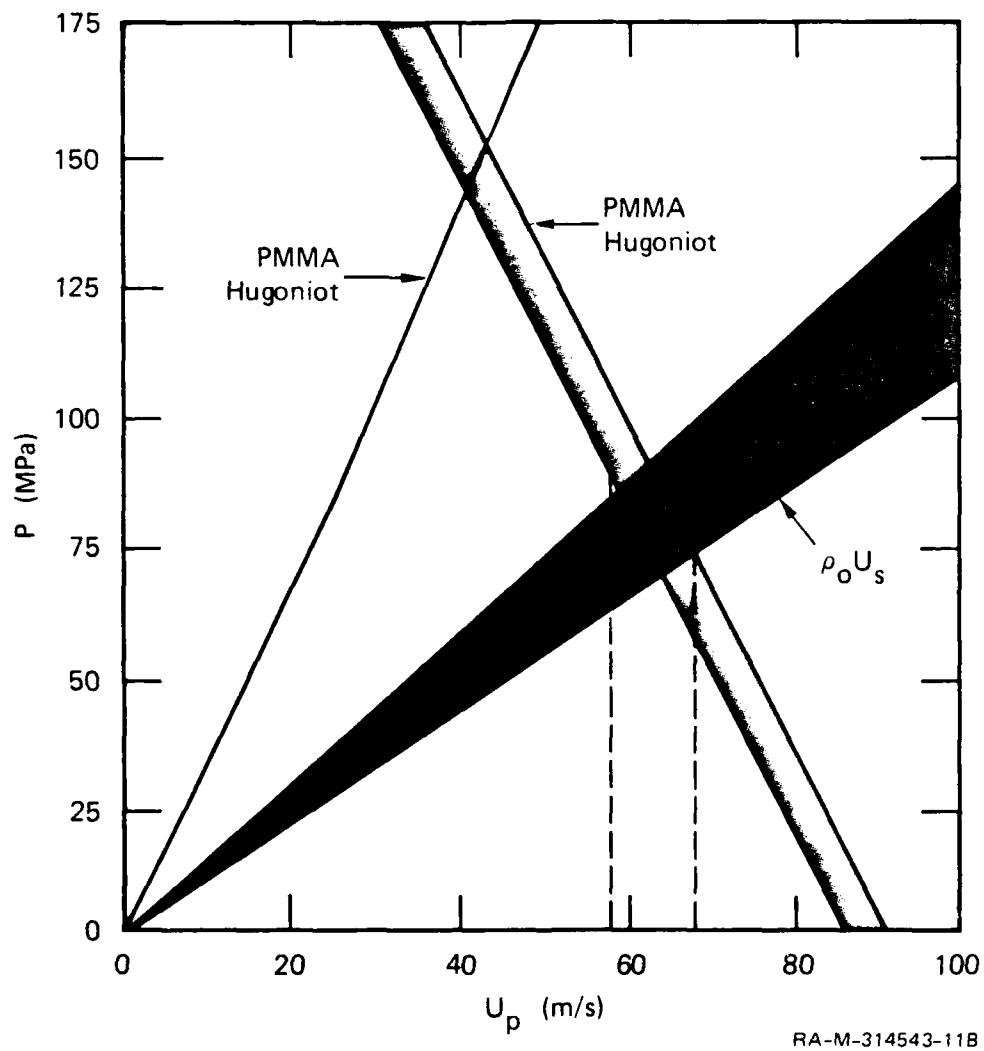
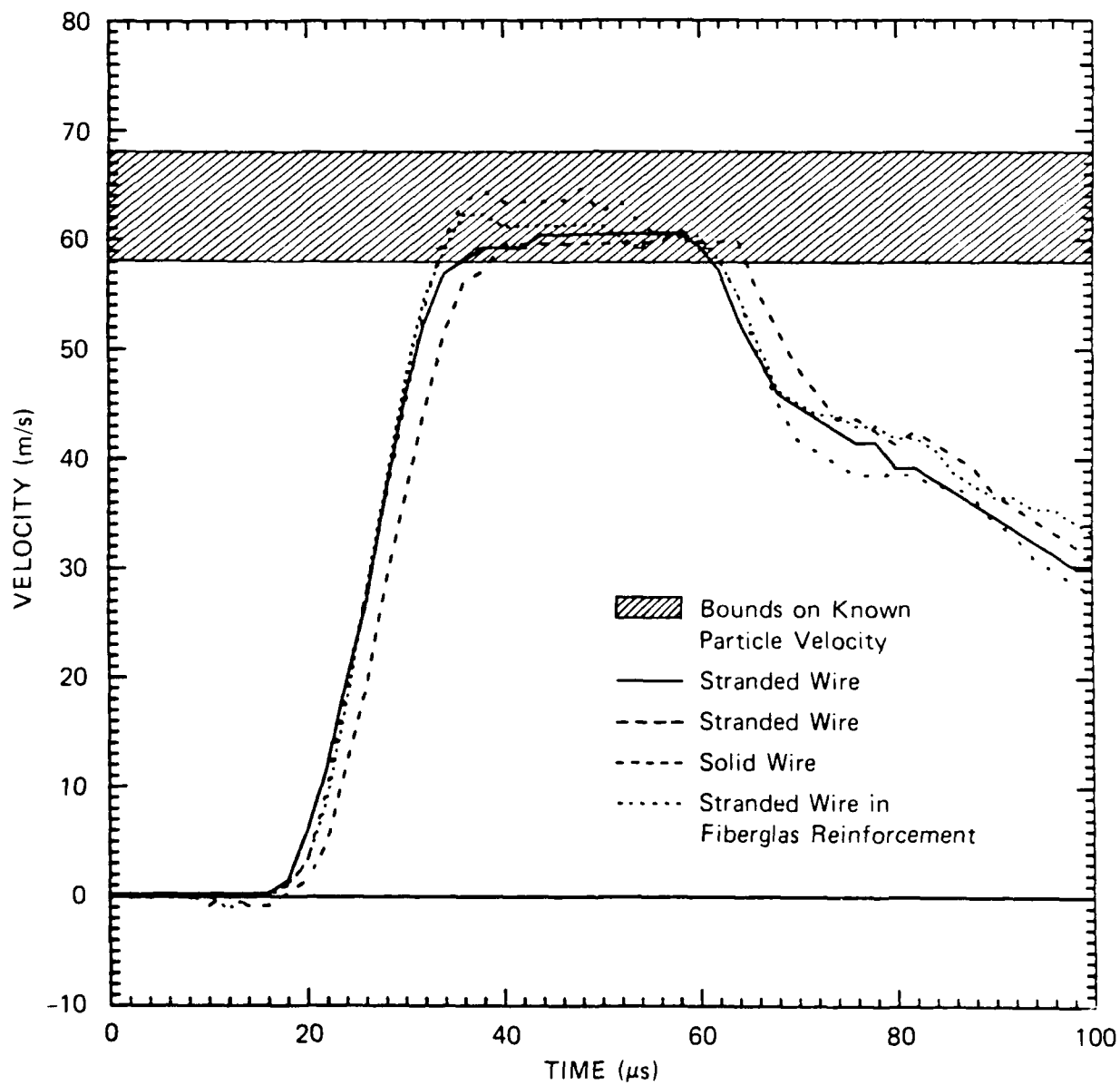


Figure 2.9. Pressure-particle velocity diagram for defining bounds on particle velocity.



RA-314543-13B

Figure 2.10. MIPV gage records in dry sand test bed.



Although all MIPV gage types performed well, the stranded wire gage showed slightly higher fidelity and therefore was chosen as the standard gage. The casket approach to gage emplacement provided the uniform density around the MIPV gage and the intimate contact between gage and test material necessary for successful gage performance.

## SECTION 3

### LARGE-DIAMETER FLYER PLATE SHOT 8-4

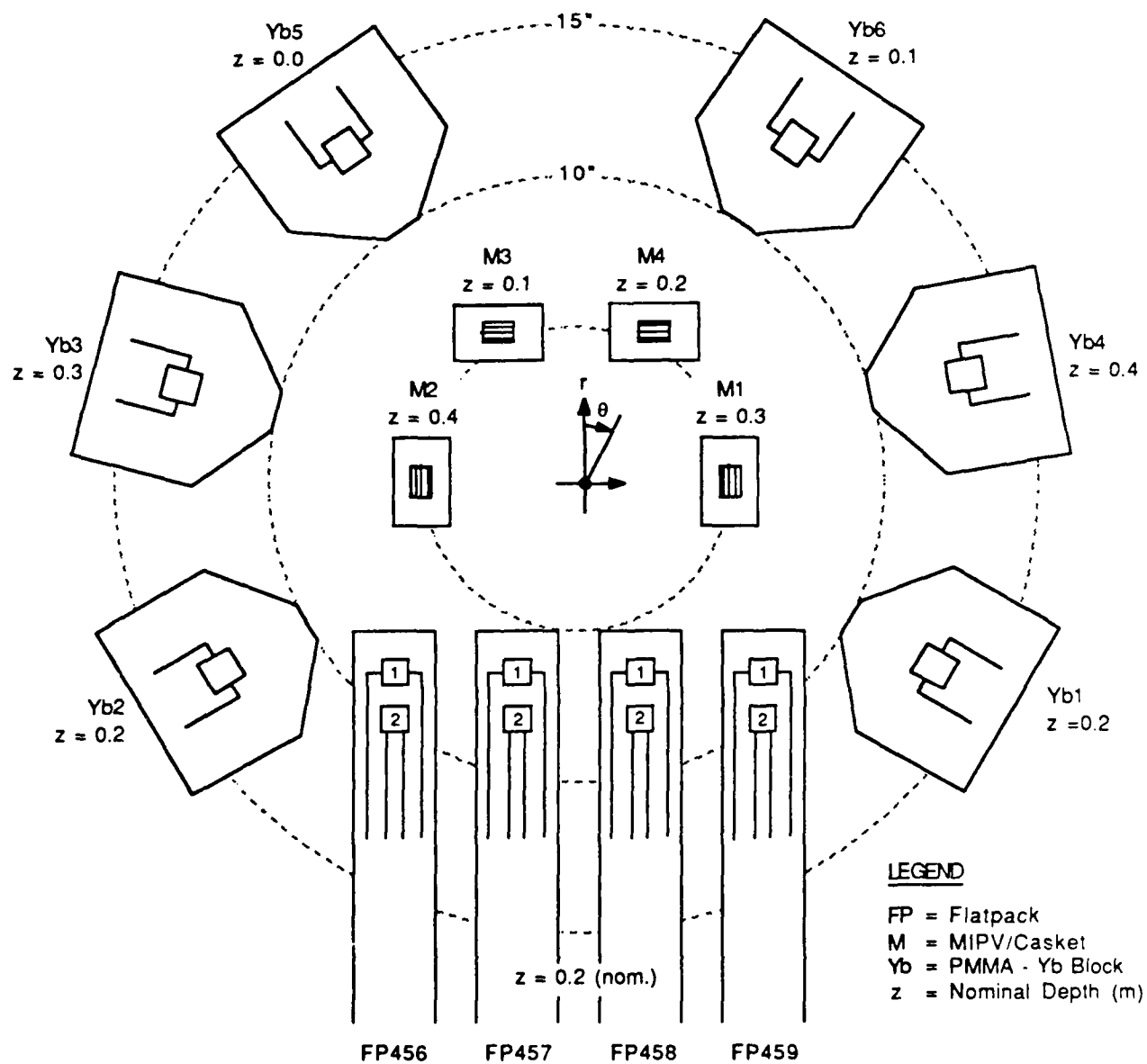
Having validated the first principles gage by an emplacement technique usable in the field (i.e., prefabricated casket modules), we can extend the validation to other experiments, namely, the AFWL large-diameter (8-foot) flyer plate calibration facility.

The primary objective of the SRI instrumentation effort in support of the AFWL 8-foot flyer plate shot 8-4 was to evaluate the performance of the flatpack stress gage in a sand test bed to a known input free-field stress history. Specifically, our approach was to (1) use the validated MIPV gage to measure particle velocity histories at different depths in the rained sand test bed, (2) perform a Lagrangian analysis on the particle velocity records to calculate the free-field input stress history, (3) measure the output of flatpack stress gages at a test bed depth where the free-field stress history is known from the Lagrangian analysis, (4) reduce the gage output to stress using a transfer function, and (5) compare the measured stress to the known input stress.

#### 3.1 EXPERIMENTAL CONFIGURATION.

The top view of the SRI instrumentation layout in the AFWL shot 8-4 is shown in Figure 3.1. We fielded six stress-wave-resolving PMMA-Yb blocks (designated Yb) at depths ranging from the impact surface to 40 cm, four flatpacks (each containing two ytterbium-sensing elements) at a depth of 20 cm in the sand test bed, and four validated MIPV gages in Plexiglas caskets at nominal depths of 10, 20, 30, and 40 cm. The specific as-built gage locations and TOA data for each gage are listed in Table 3.1.

The PMMA-Yb blocks are shown in Figure 3.2 and were used to (1) measure the time of wave arrival and (2) resolve the front end of the input waveform and determine if effects such as an airshock precursor could trigger other TOA diagnostic closure pins. We fielded four flatpack stress gages, each containing two piezoresistant ytterbium elements, at a nominal depth of 20 cm from the impact surface. A schematic of the flatpack stress gage is shown in Figure 3.3. Two flatpacks, designated 'S' in Table 3.1, were the standard design, using Kapton encapsulant and spray adhesive to mount the ytterbium element. Two flatpacks, designated 'N' in Table 3.1, were a developmental gage design using a Teflon encapsulant and epoxy to mount the ytterbium elements, and were not evaluated for



RA-M-314543-10A

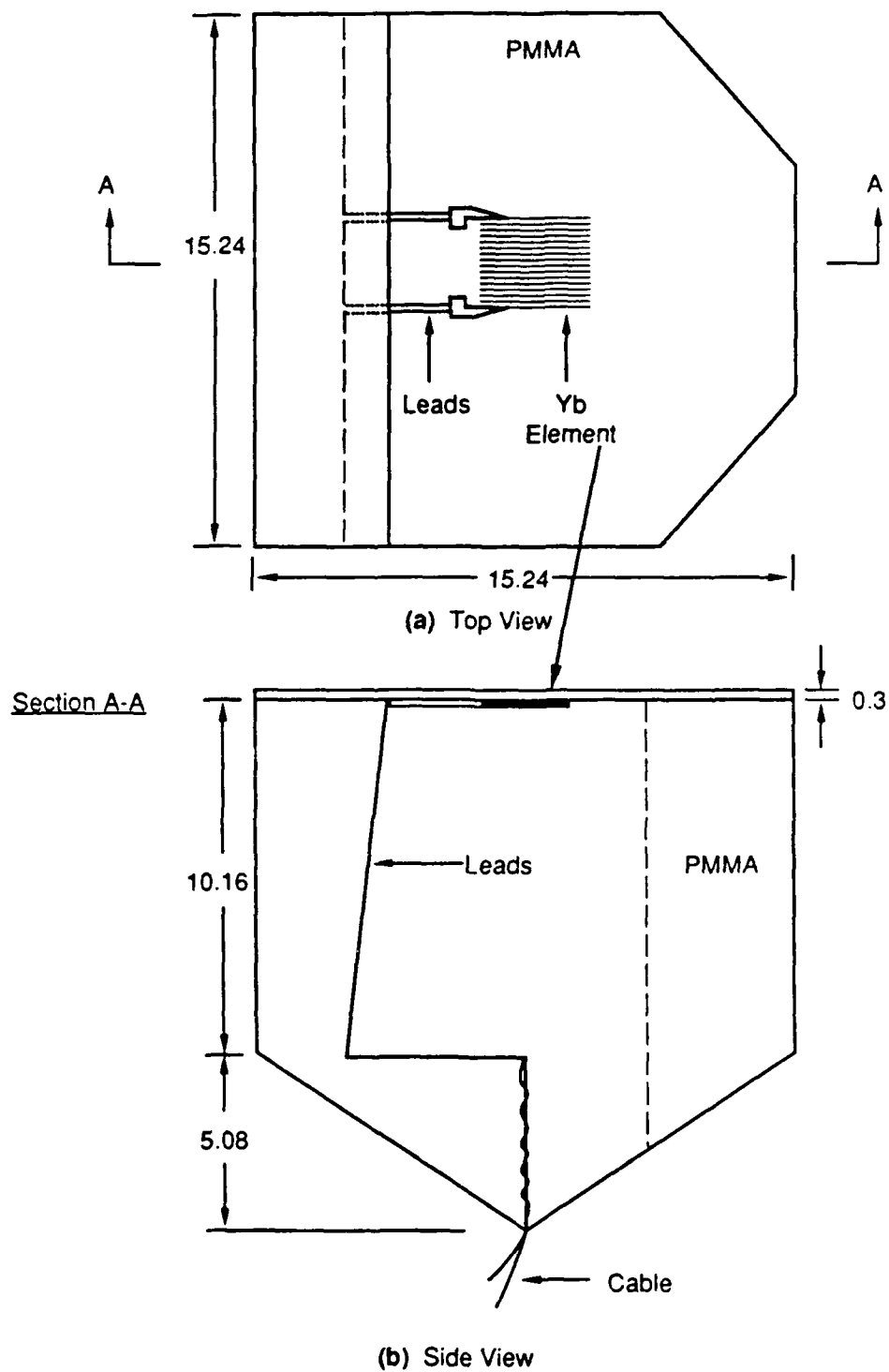
Figure 3.1. SRI instrumentation layout in AFWL large flyer plate shot 8-4.

Table 3.1. As-built gage locations for SRI instrumentation in  
8-foot flyer plate experiment 8-4.

<u>Gage No.</u>	<u>Radius R (m)</u>	<u>Angle (deg)</u>	<u>Depth Z (m)</u>
YB 1	0.33	122	0.199
YB 2	0.33	238	0.199
YB 3	0.33	277	0.304
YB 4	0.33	83	0.401
YB 5	0.33	320	0.0
YB 6	0.33	35	0.092
FP456-1 <sup>a</sup> (N) <sup>b</sup>	0.188	228	0.214
FP456-2 (N)	0.188	228	0.214
FP457-1 (N)	0.137	199	0.210
FP457-2 (N)	0.137	199	0.210
FP458-1 (S)	0.137	161	0.211
FP458-2 (S)	0.137	161	0.211
FP459-1 (S)	0.188	132	0.213
FP459-2 (S)	0.188	132	0.213
MIPV1	0.127	90	0.311
MIPV2	0.127	270	0.4077
MIPV3	0.137	326	0.1024
MIPV4	0.137	34	0.2217

<sup>a</sup>Element 1 or element 2 as shown in Figure 3.1.

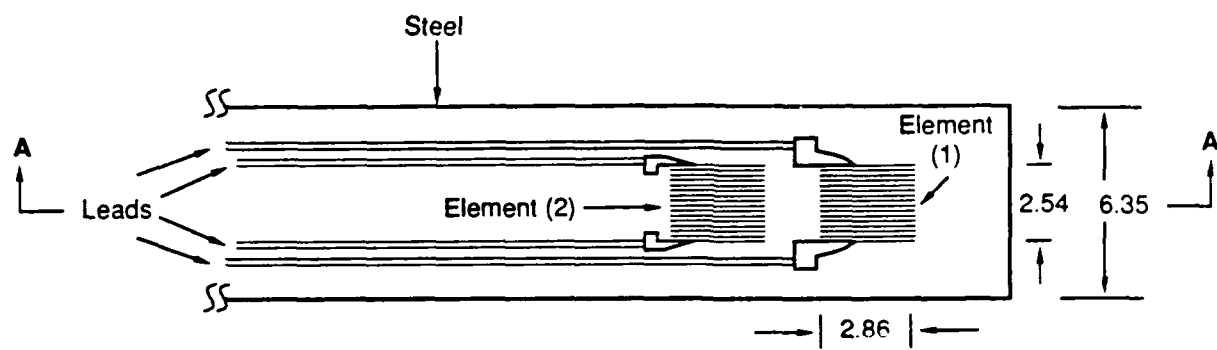
<sup>b</sup>(N) = New flatpack design; (S) = standard flatpack.



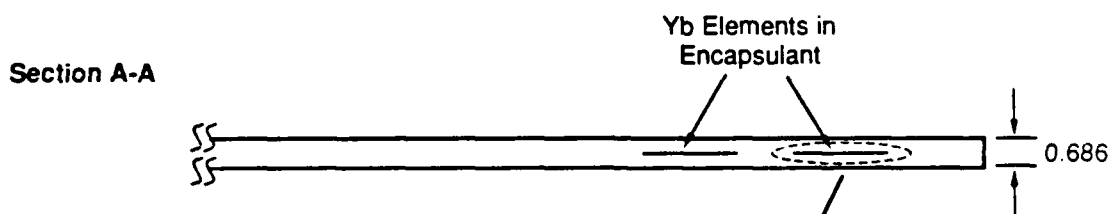
NOTE: Dimensions in cm.

RA-M-314582-5

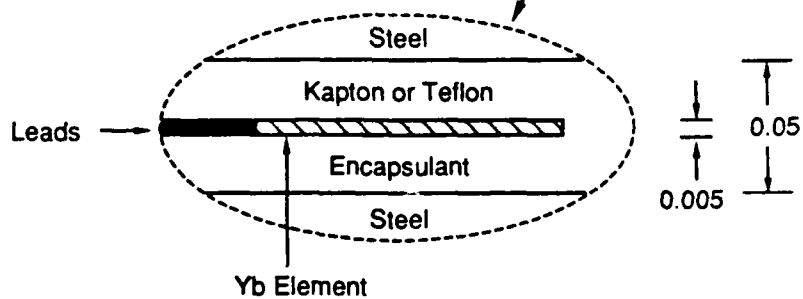
Figure 3.2. Ytterbium element in PMMA block, used for TOA/peak stress measurement in rained sand test bed shot 8-4.



(a) Top View



(b) Side View



(c) Side view of Yb element in encapsulant

NOTE: Dimensions in cm.

RA-M-314582-3

Figure 3.3. Schematic of flatpack stress gage used in large flyer plate shot 8-4.

this experiment. We fielded four validated MIPV gages in Plexiglas caskets, shown in Figure 3.4, at nominal depths of 10, 20, 30, and 40 cm in the test bed.

The flatpacks and MIPV gage locations in the test bed are shown in side view in Figure 3.5. The MIPV gages were mounted in caskets, and we rained sand around the gage to fill the casket before it was sealed and placed into the test bed. The flatpacks were bent 46 cm from the front of the gage and came out the side of the test bed through a trench. The estimated uniaxial strain region in the test bed is also shown in that figure.

The sand used in the test bed was medium-grit sand blasting sand with a reported rained density of about  $1.63 \text{ g/cm}^3$  and moisture content of about 0.2%.

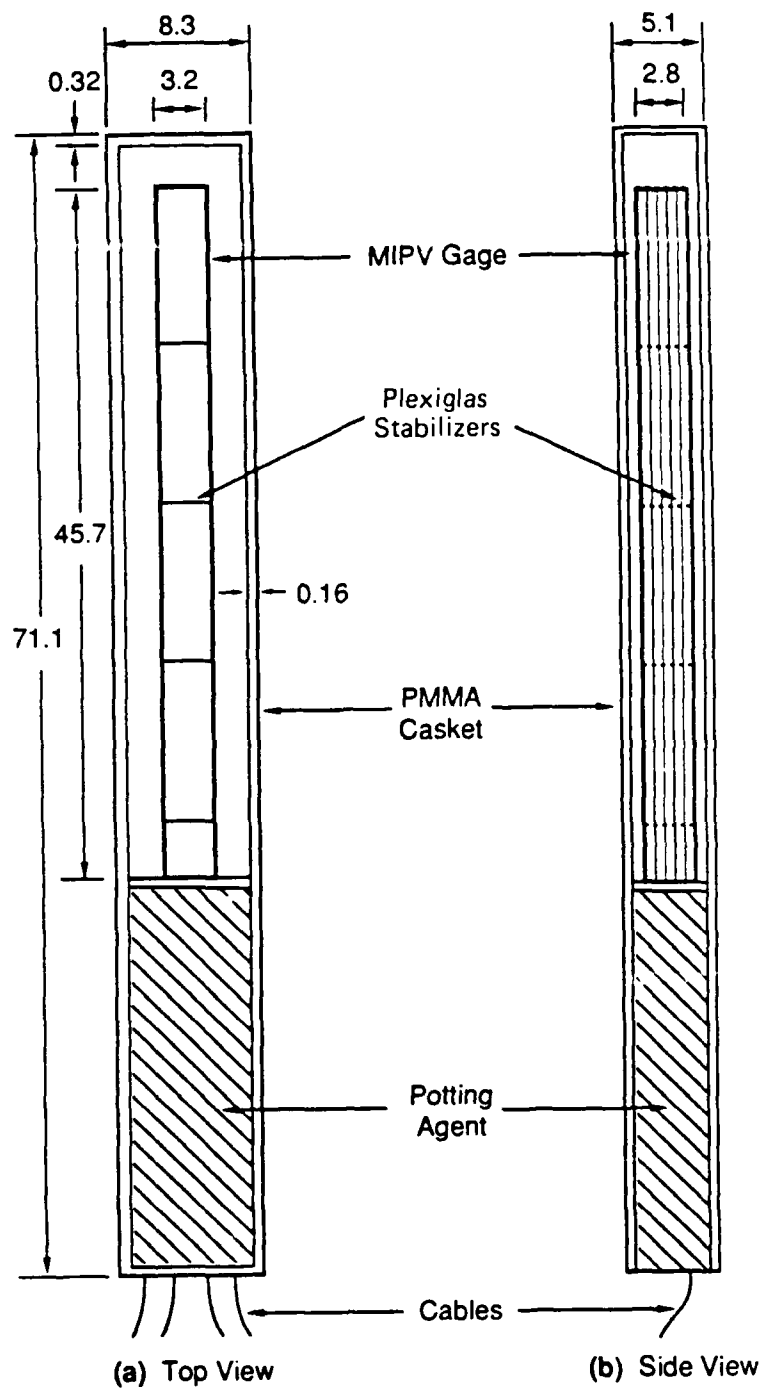
### 3.2 EXPERIMENTAL RESULTS.

The results of the MIPV gages are given as particle velocity histories in Figure 3.6. The records are terminated 500  $\mu\text{s}$  after TOA, coinciding with the calculated shock wave arrival at the sand/potting material interface within the casket. These records have been filtered at 150 kHz and an attenuation rate of 10 dB/octave because the unfiltered data contained noise that was not part of the gage signal. Unfiltered, high-fidelity Nicolet oscilloscope records for the front end of the signal are shown in Figure 3.6(b). These records were cut short in the experiment owing to an unannounced change in shot timing, but we used these records as a guide in the filtering process to preserve at least 95% of the rise time and peak amplitude, as shown in the records in Figure 3.6(a).

### 3.3 FREE-FIELD STRESS FROM LAGRANGE ANALYSIS.

Lagrangian analysis is a procedure for deriving the stress-strain relations for a material from the stress or particle velocity histories measured during the passage of a one-dimensional stress wave through the material. Detailed explanations of the procedure are available in the literature.<sup>4</sup>

We performed a Lagrangian analysis of the first two particle velocity histories obtained from shot 8-4 to calculate the free-field stress at a depth of 20 cm, which coincides with the location of the flatpack stress gages. The particle velocity record obtained from the 30-cm depth was not included in the analysis because of an anomalous rise not observed in the other records, namely, a kink in the record near the peak. This anomaly can be seen in the high-fidelity Nicolet scope records in Figure 3.6(b). Because the analysis is valid only in uniaxial flow fields, we did not include the gage at the 40-cm depth since, as shown in Figure 3.5, this gage was outside the uniaxial strain region.

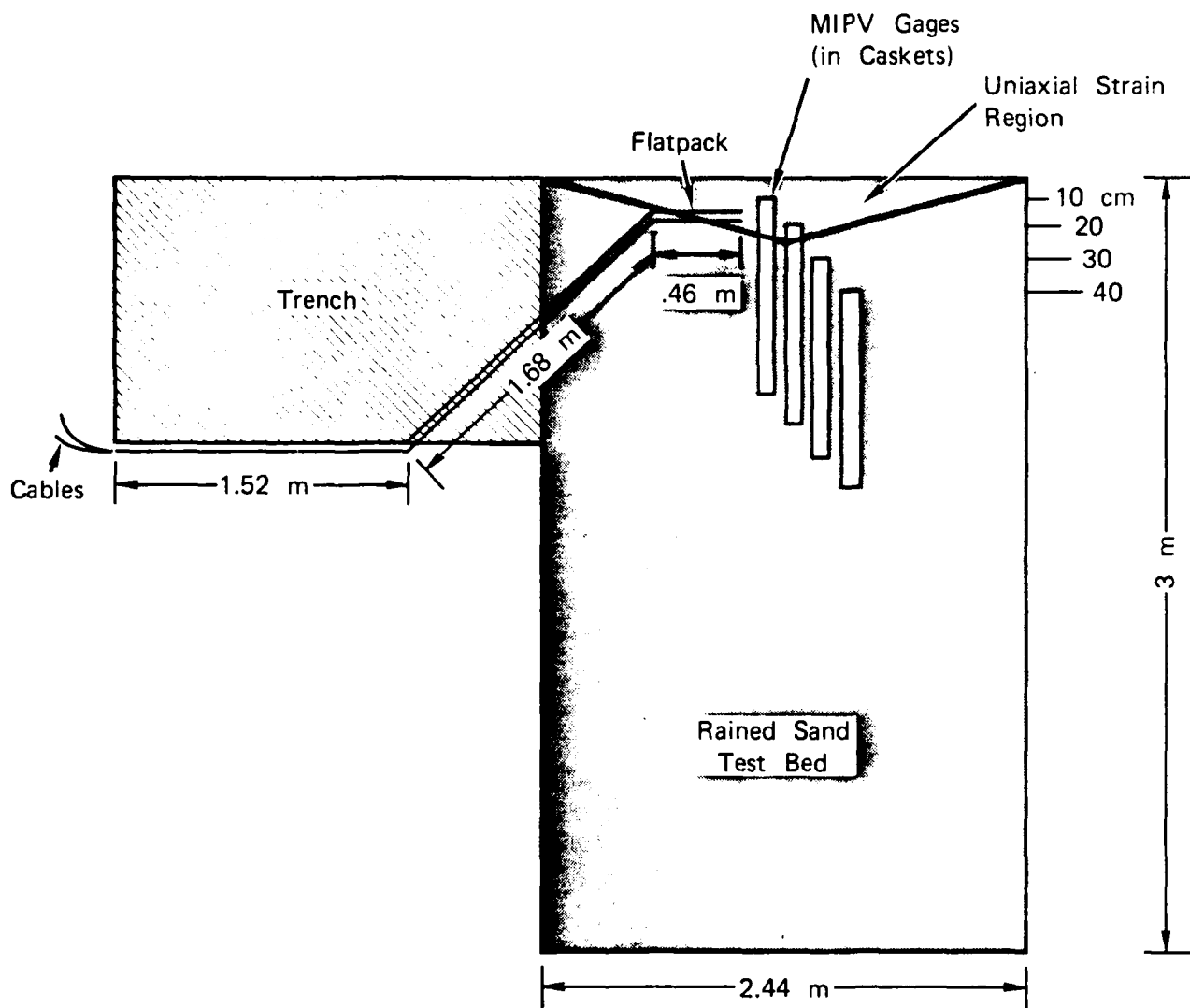


NOTE: Dimensions in cm.

RA-M-314582-2

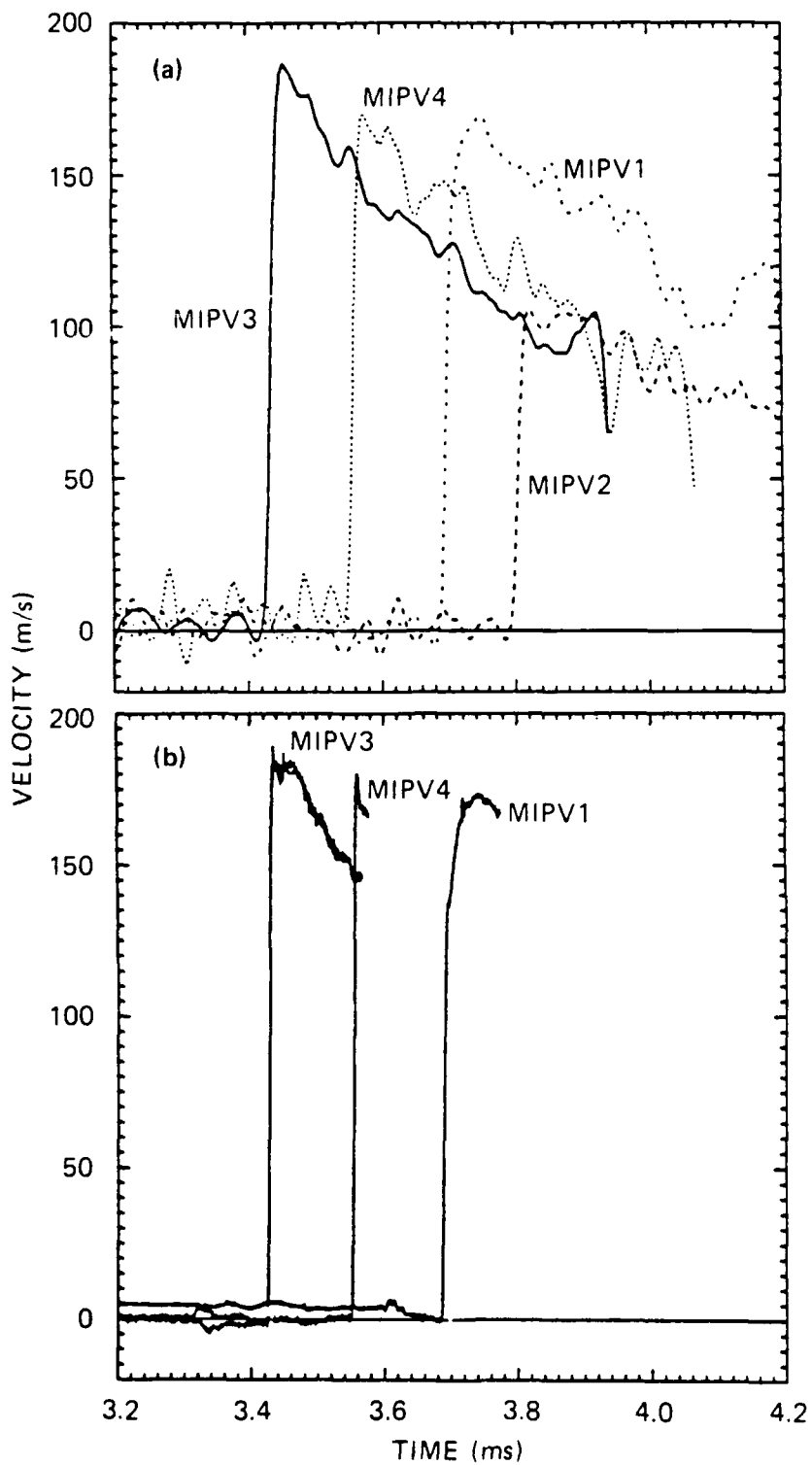
Figure 3.4. MIPV gage in PMMA casket used in dry sand test bed shot 8-4.





RA-2721-5

Figure 3.5. Side view of instrumentation layout in rained sand test bed shot 8-4.



RA-314582-26b

Figure 3.6. MIPV gage records obtained from 8-foot (2.4-m) flyer plate shot 8-4.  
 (a) Tape records filtered at 150 kHz.  
 (b) Unfiltered Nicolet oscilloscope records.

The results for the first 200  $\mu$ s of the pulse are shown in Figure 3.7, indicating a peak stress at the 20-cm depth of about 300 MPa. The shaded region in the figure represents the uncertainty bounds in the particle velocity measurement determined from the MIPV gage validation experiment.

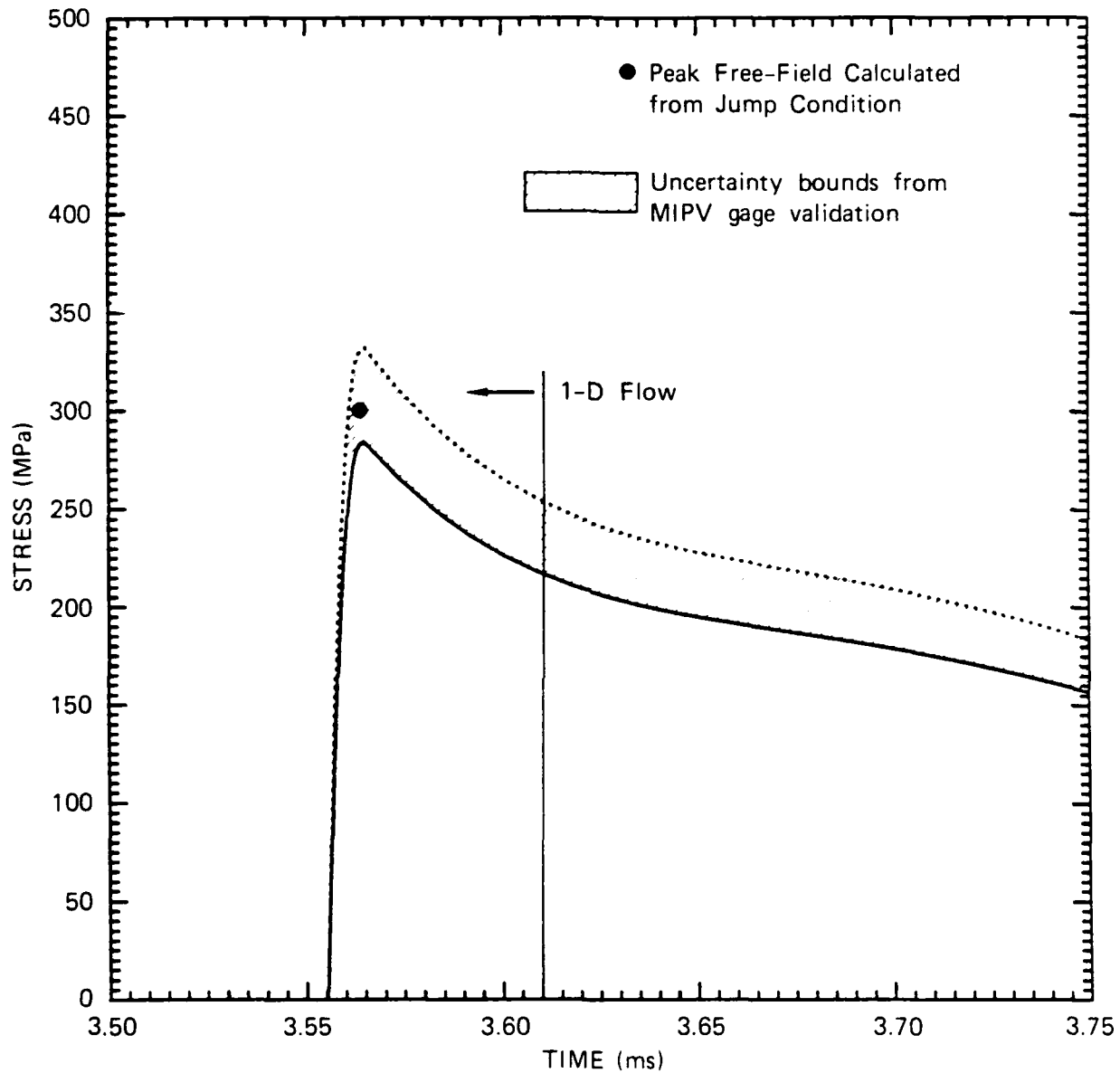
#### 3.4 COMPARISON OF KNOWN AND MEASURED FREE-FIELD STRESS.

We reduced the gage output of the standard flatpacks ( $\Delta R/R_0$ ) to stress using the transfer function data reduction procedure described in the Section 4.3.2. The measured stress results are shown superimposed on the free-field stress calculated from the Lagrangian analysis in Figure 3.8. As shown in the figure, the initial stress in the gage overshoots the free-field stress by about a factor of 3. This overshoot results from a large difference in impedance between the sand test bed and the steel flatpack, and the response of the gage under this condition is described in further detail in Section 4.3.2. After the initial overshoot, the measured stress shows a systematic underregistration of the free-field stress, followed by differences ranging from 5% to 20%.

Because the gage represents an inclusion in the sand test bed matrix, the measured stress history shown in Figure 3.8 is actually the stress in the gage package and not the free-field stress. Therefore, the gage signal due to the mechanical response of the flatpack inclusion must be separated from the signal due to the free-field loading history. An approximate technique for separating these two effects is to develop a filter function characteristic to the flatpack's oscillation response to a specific input and filter this effect from the gage record. We briefly summarize this technique: a full explanation is given in Reference 3.

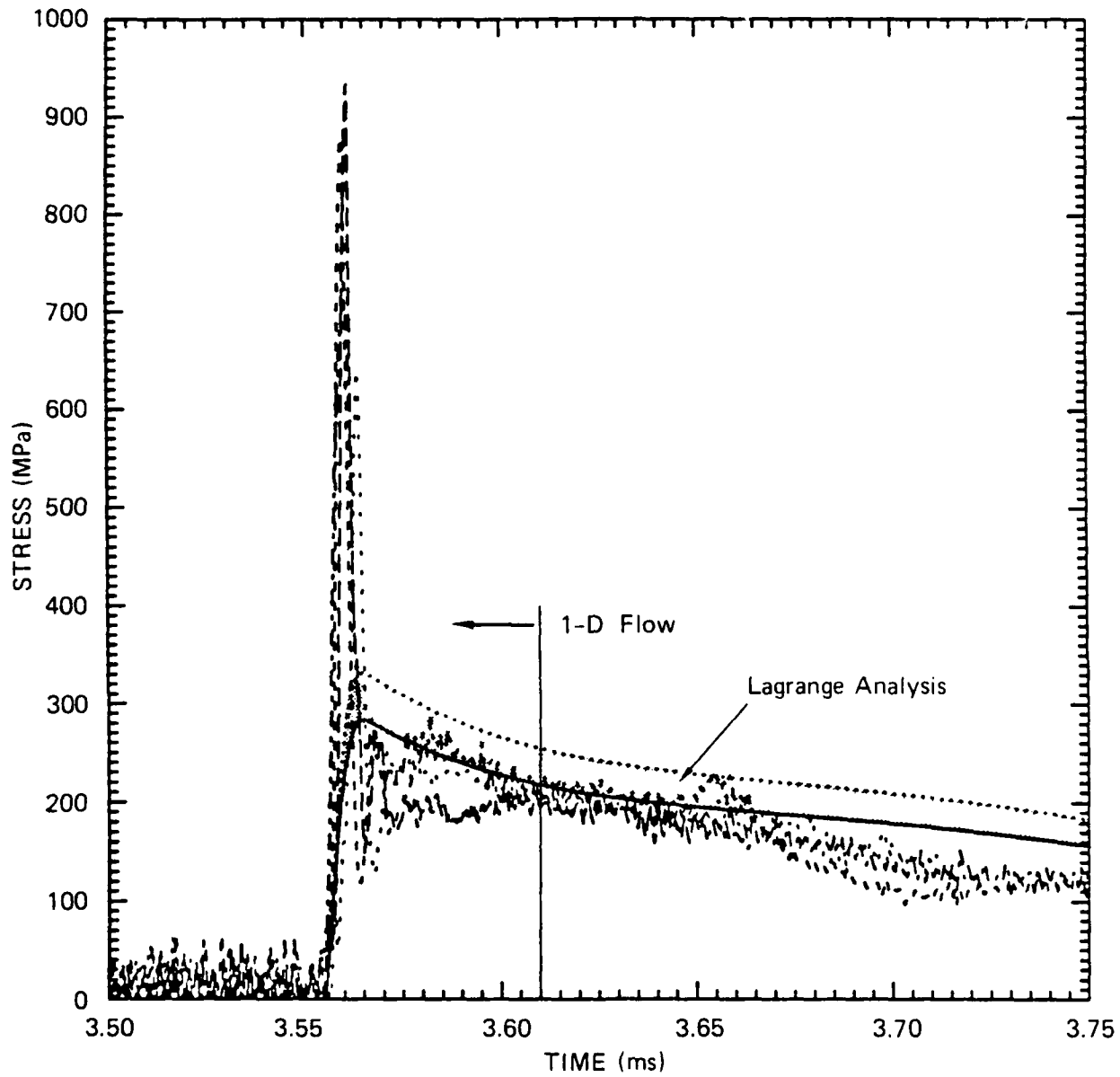
The mechanical response of the flatpack gage can be determined by applying a known input and measuring the output. We performed an experiment in which a flatpack in PMMA was subjected to a square wave input, and the output of the gage was a damped oscillation. We then developed a filter function characteristic to this particular gage design. If we assume that the flatpack mechanical response is primarily a function of the gage components (steel and insulator) and geometry (steel and insulator thickness) and that the effects resulting from the surrounding material on the oscillation response of the gage are second-order, then we can apply this technique to the experimental records from shot 8-4.

We applied the filter function derived for the standard flatpacks to the records shown in Figure 3.8, and we show the results in Figures 3.9(a) and (b).



RA-314543-19A

Figure 3.7. Early-time stress history computed from Lagrange analysis at 20-cm depth in sand test bed for 8-foot (2.4-m) flyer plate shot 8-4.



RA-314543-18A

Figure 3.8. Comparison of flatpack gage stress histories with free-field stress history calculated from Lagrange analysis.

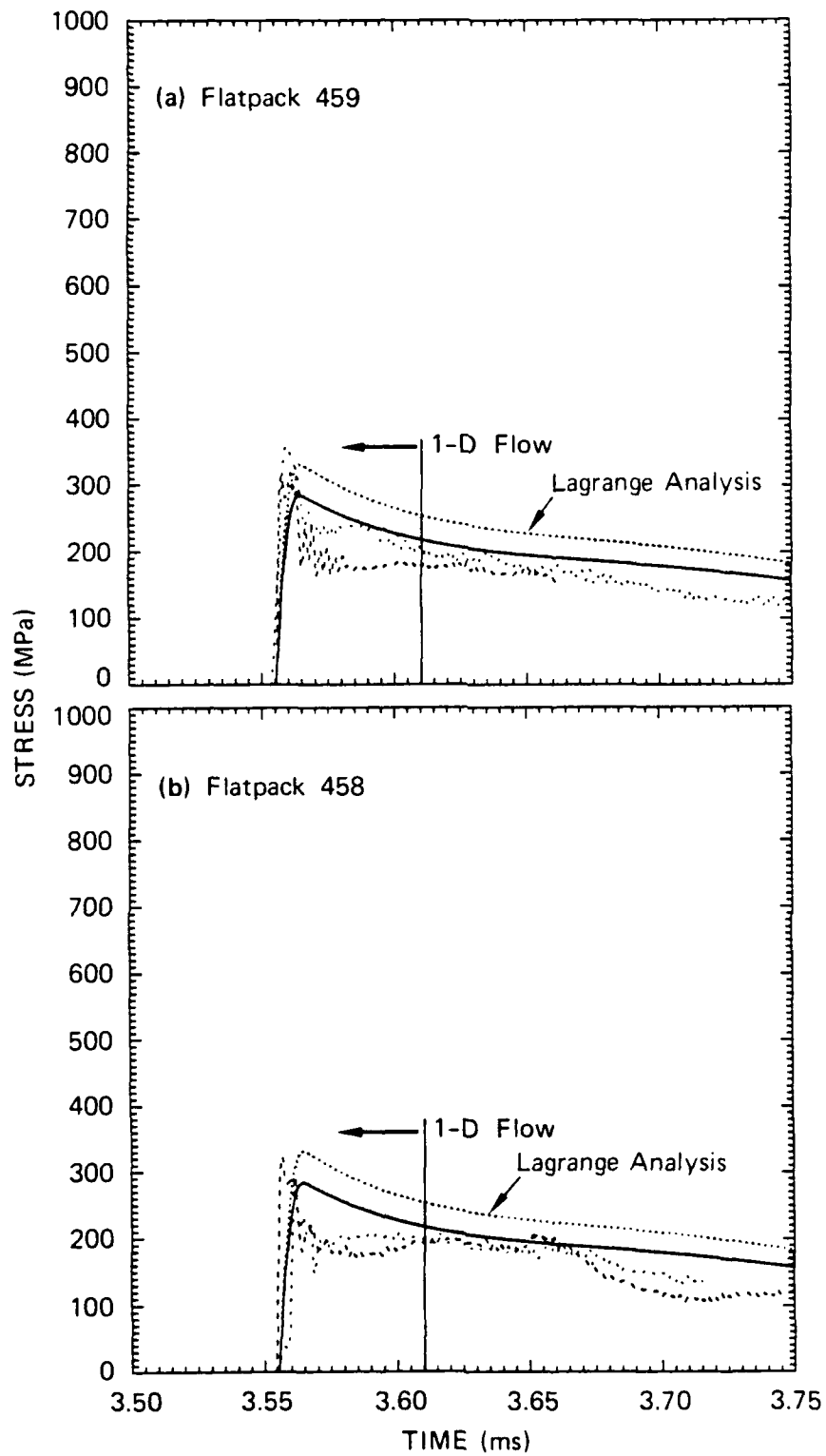
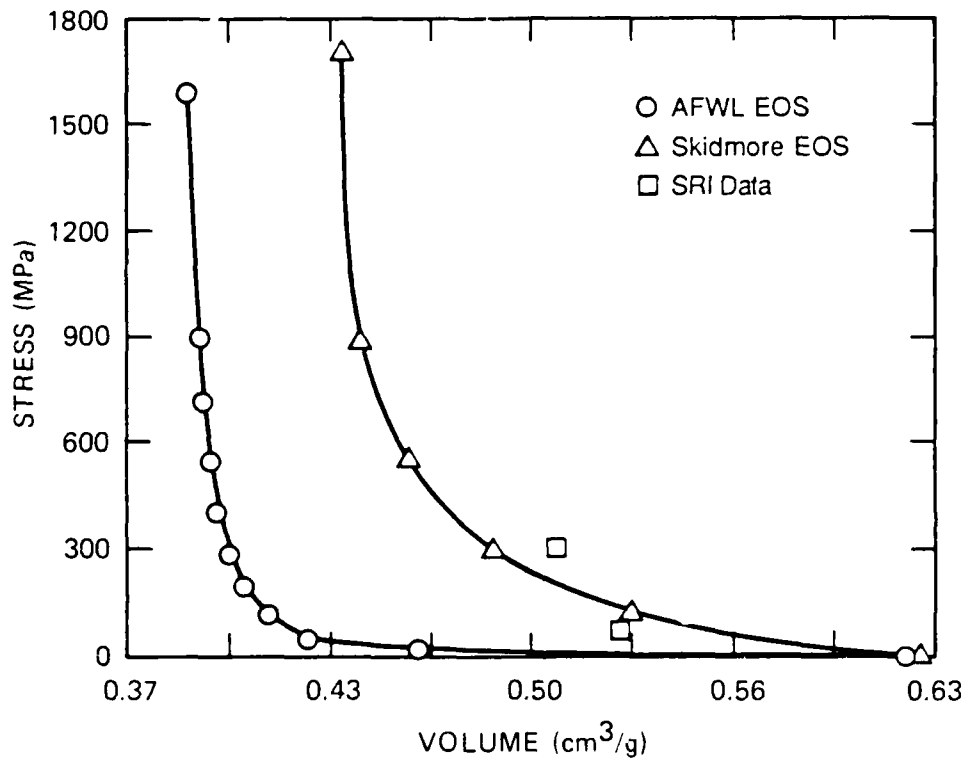


Figure 3.9. Comparison of flatpack stress histories using filter function and calculated stress history from Lagrange analysis.

Depth of 20-cm in sand test bed shot 8-4.

By applying this procedure to the flatpack records, we significantly reduced the overshoot due to the gage inclusion, and all the records show a peak stress within the stress bounds determined from the Lagrangian analysis. The applicability of the filter function derived from a square wave input in PMMA to an attenuating wave in sand remains uncertain, but the consistent peak stress calculated from the Lagrangian analysis and measured by the flatpacks is encouraging. After the peak stress, the flatpack shows the same systematic underregistration of the calculated stress observed before application of the filter function. We are unsure of the reason for this underregistration, but one possibility is the arrival of two-dimensional effects of the edge release waves in the test bed. The estimated arrival of two-dimensional effects shown in Figures 3.7 through 3.9 was determined using the average release wave velocity of the sand (4.05 mm/ $\mu$ s) and assuming negligible tilt and flyer plate deflections. Because of the large uncertainties in both the arrival and magnitude of the two-dimensional effects, these effects should be monitored in subsequent experiments.

The 300-MPa peak stress at the 20-cm depth calculated from the Lagrangian analysis differs from the 420-MPa peak stress reported in separate analyses.<sup>5,6</sup> The basis for the contradiction may reside in the material model used for interpreting TOA and strain can measurements used for calculating stress. This discrepancy is shown in the pressure-volume (P-V) curve for the sand in Figure 3.10. The open circles represent the P-V relation for the sand model determined from Hopkinson bar data<sup>7</sup> used in the locking solid model by the AFWL, the open triangles are the Hugoniot points from an extrapolation of EOS measurements of dry sand performed by Skidmore,<sup>8</sup> and the open squares are the data obtained by SRI from the 2-foot gas gun experiment on dry sand and determined from flyer plate shot 8-4. The discrepancy in the material model could be resolved with uniaxial strain equation of state measurements of the sand used in the 8-foot flyer plate test bed.



RA-5467-9A

Figure 3.10. Comparison of AFWL EOS with Skidmore EOS and SRI data.



## SECTION 4

### COMPUTATIONAL MODEL OF FLATPACK RESPONSE AND DATA REDUCTION PROCEDURES

The current empirical method of reducing flatpack data could be significantly enhanced by the development of a computational model of the flatpack response. The computational model is based on an electromechanical model of piezoresistance (EP model) developed by Gupta<sup>9</sup> for the ytterbium element and on standard material models for the other components of the gage (steel, insulator, etc.). We performed a gage calibration experiment of flatpacks and their components in a PMMA target for the purpose of generating flatpack response data to a well-defined input loading history to evaluate the current state of the model and also of enhancing our understanding of the transfer function (calibration curve) approach to reducing flatpack data. A secondary objective was to determine the effects of different insulators and ytterbium element mounting agents on the gage output, and we investigated two specific variations: (1) elements mounted with spray adhesive in a Kapton insulator, the standard flatpack insulator/mounting agent combination and (2) elements mounted with epoxy in either Kapton or Teflon insulators.

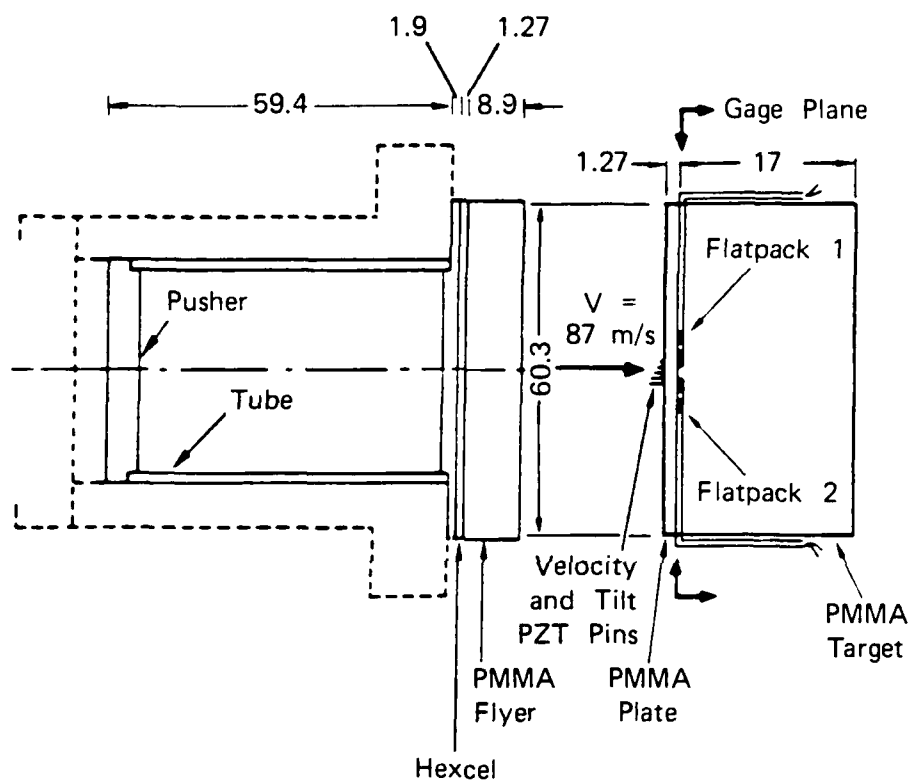
#### 4.1 EXPERIMENTAL CONFIGURATION.

The gage calibration experiment was performed in the SRI 2-foot gas gun facility described in Section 2, and the experimental configuration is shown in Figure 4.1. In this experiment, a PMMA flyer plate impacted a PMMA target containing two flatpack stress gages (armored) and five ytterbium elements encapsulated in an insulator (unarmored). The gage layout is shown in the front view of the target in Figure 4.2, and the specific insulator and mounting agent for the gages are listed in Table 4.1.

Because the experiment was a symmetric impact of a well-characterized material (PMMA), the stress amplitude can be defined by simply measuring the flyer plate velocity at impact. We measured an impact velocity of  $86.5 \pm 2$  m/s, generating a shock wave in the target and flyer plate with a stress amplitude of  $148 \pm 3$  MPa.

#### 4.2 EXPERIMENTAL RESULTS.

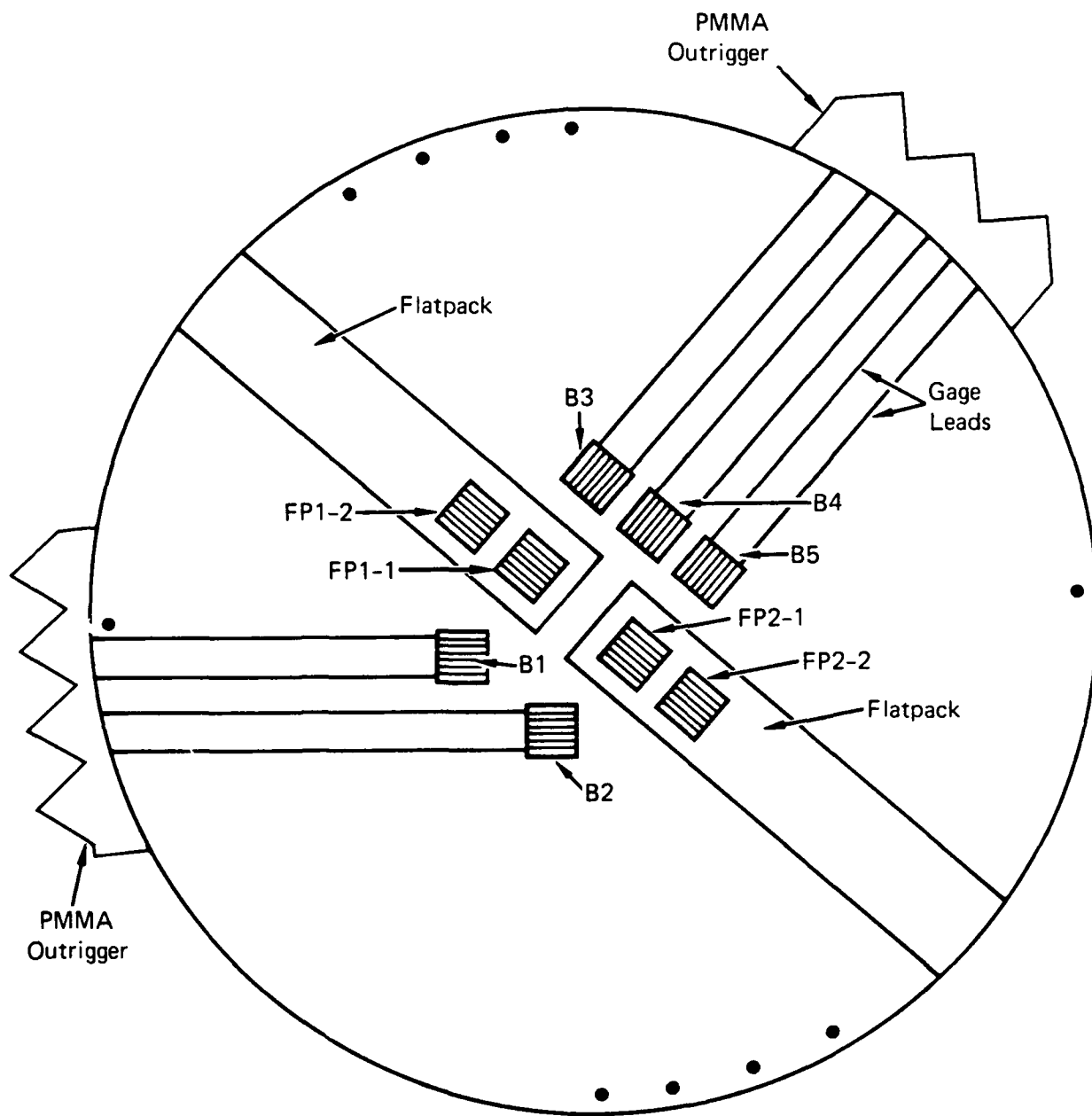
The relative resistance change ( $\Delta R/R_0$ ) records for the five (unarmored) encapsulated elements are shown superposed in Figure 4.3. Zero time is referenced from the oscilloscope triggering, about  $13 \mu\text{s}$  before impact. We observe that the



JA-8270-336B

Figure 4.1. Configuration for 24-inch (60.9-cm) gas gun calibration experiment in PMMA, showing two field flatpacks.

Refer to Figure 4.2 for complete gage layout.  
Dimensions in cm.

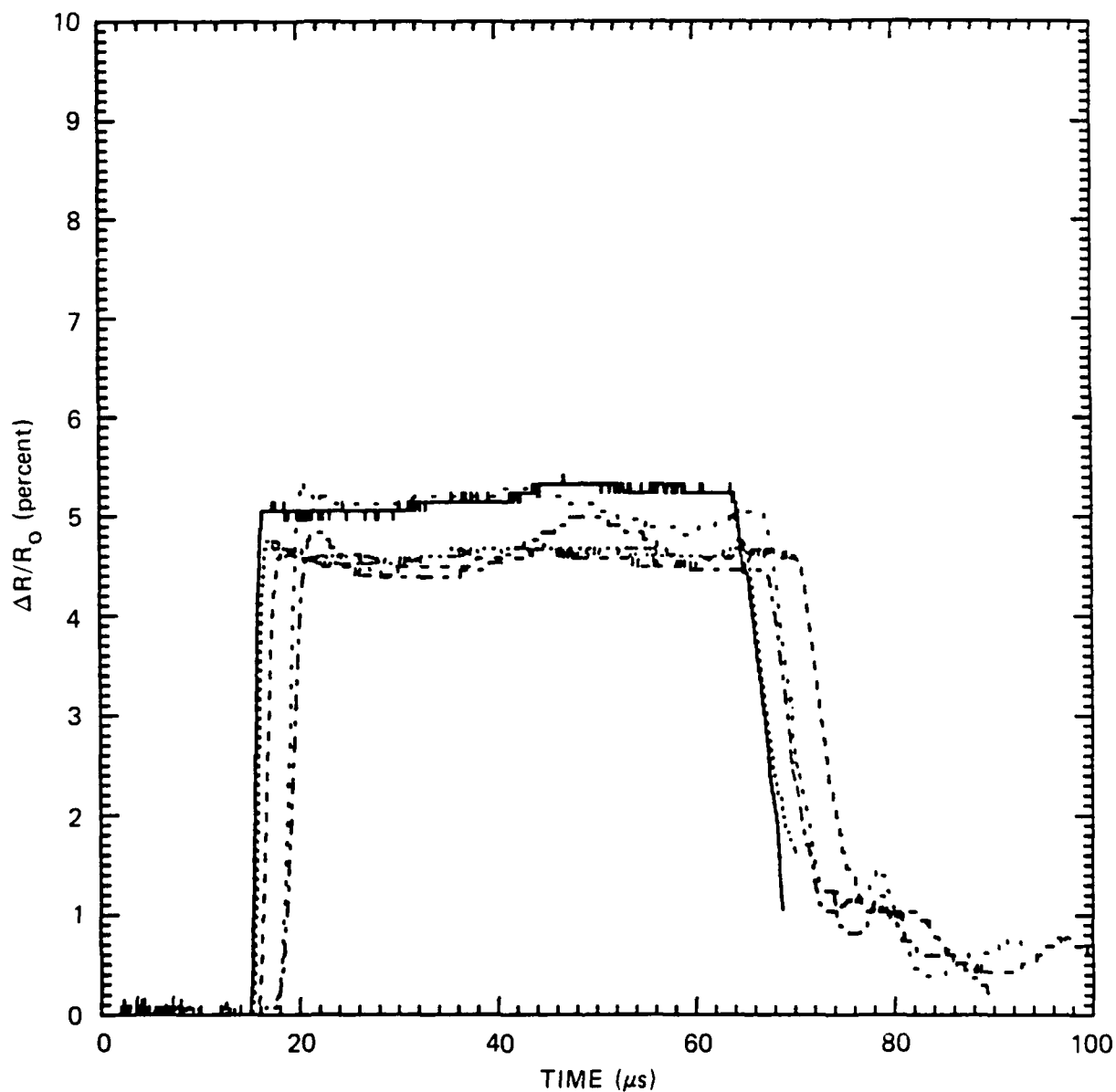


● Velocity and Tilt Pins

RA-2721-6

Figure 4.2. Front view of layout in gage calibration experiment.

Refer to Table 4.1 for gage description.



RA-2721-7

Figure 4.3. Composite relative resistance change records for encapsulated gages (B1-B5) obtained from gage calibration experiment in PMMA.

square wave input generated by the plate impact/flyer plate free-surface is represented by these records. The relative resistance change records from the elements inside the flatpack, on the other hand, show a different character, namely, damped oscillations of the gage during the equilibrium process of the gage inclusion and the PMMA matrix, shown in Figures 4.4 (a) and (b).

Table 4.1. Front view of layout in gage calibration experiment.

<u>Gage</u>	<u>Type</u>	<u>Insulator</u>	<u>Mounting Agent</u>
FP1-1	a	a	-
FP1-2	Die-cut	Teflon	Epoxy
FP2-1	Photo-etched	Kapton	Epoxy
FP2-2	Photo-etched	Kapton	Spray adhesive
B1	Die-cut	Teflon	Epoxy
B2	Die-cut	Teflon	Epoxy
B3	Photo-etched	Kapton	Spray adhesive
B4	Die-cut	Kapton	Spray adhesive
B5	Photo-etched	Kapton	Epoxy

---

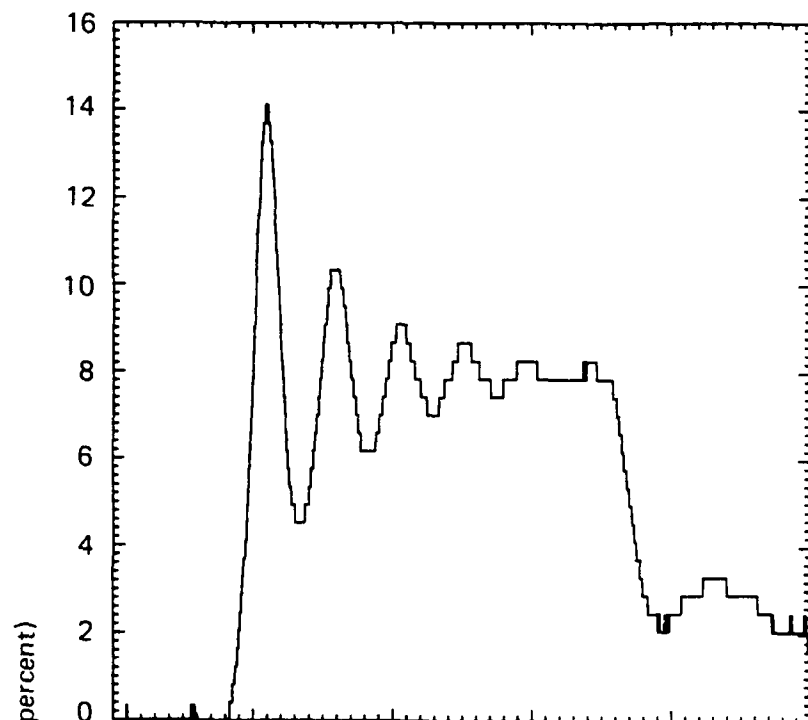
<sup>a</sup>Gage failed before to test.

A comparison of the gage output from flatpacks and the gage output from the encapsulated elements is shown in Figures 4.5 and 4.6 for different insulator/mounting agent combinations. This comparison demonstrates that the ytterbium element is sensitive to the higher initial stress inside the flatpack gage, caused by the different impedance of the steel inclusion and PMMA matrix. The different loading path affects the final equilibrium relative resistance change level achieved.

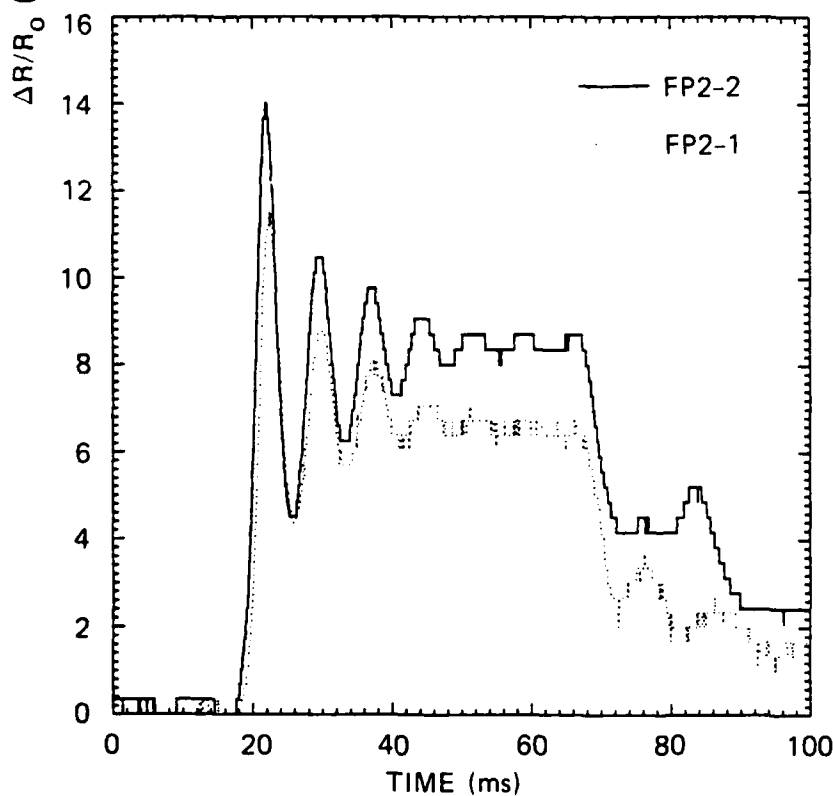
#### 4.3 RESULTS OF CALCULATING THE PMMA EXPERIMENT.

##### 4.3.1 Computational Model.

The computational model of flatpack response is based on the material models for the components of the flatpack (steel and insulator) and on an electromechanical model of piezoresistance developed by Gupta<sup>9</sup> for the ytterbium element. We performed two one-dimensional finite difference simulations of the experimental configuration shown in Figure 4.1. In the first simulation, we calculated the



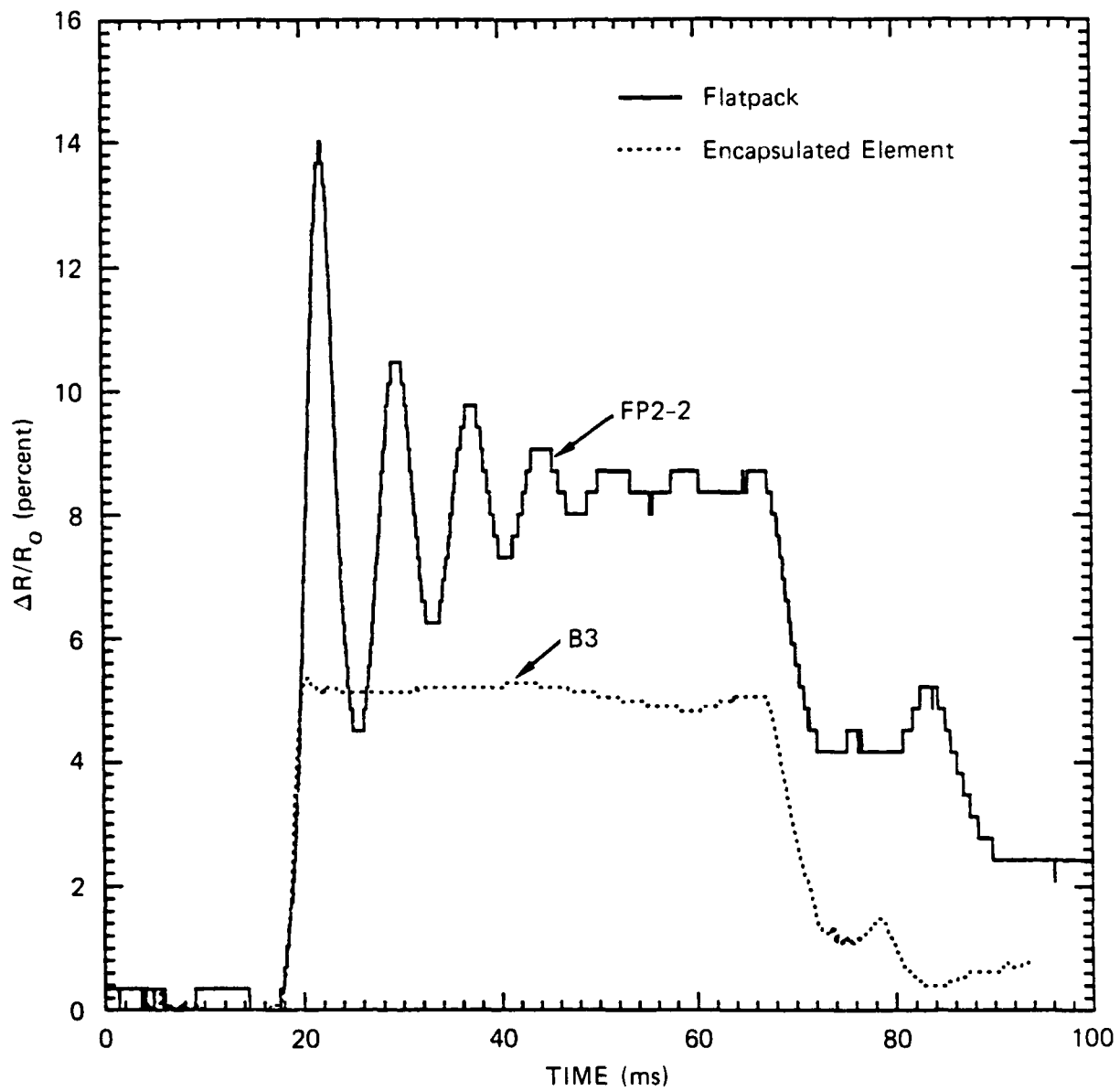
(a) Gage FP1-2  
(Teflon/epoxy  
encapsulant)



(b) Gage FP2-2  
(Kapton/adhesive encapsulant)  
Gage FP2-1  
(Kapton/epoxy encapsulant)

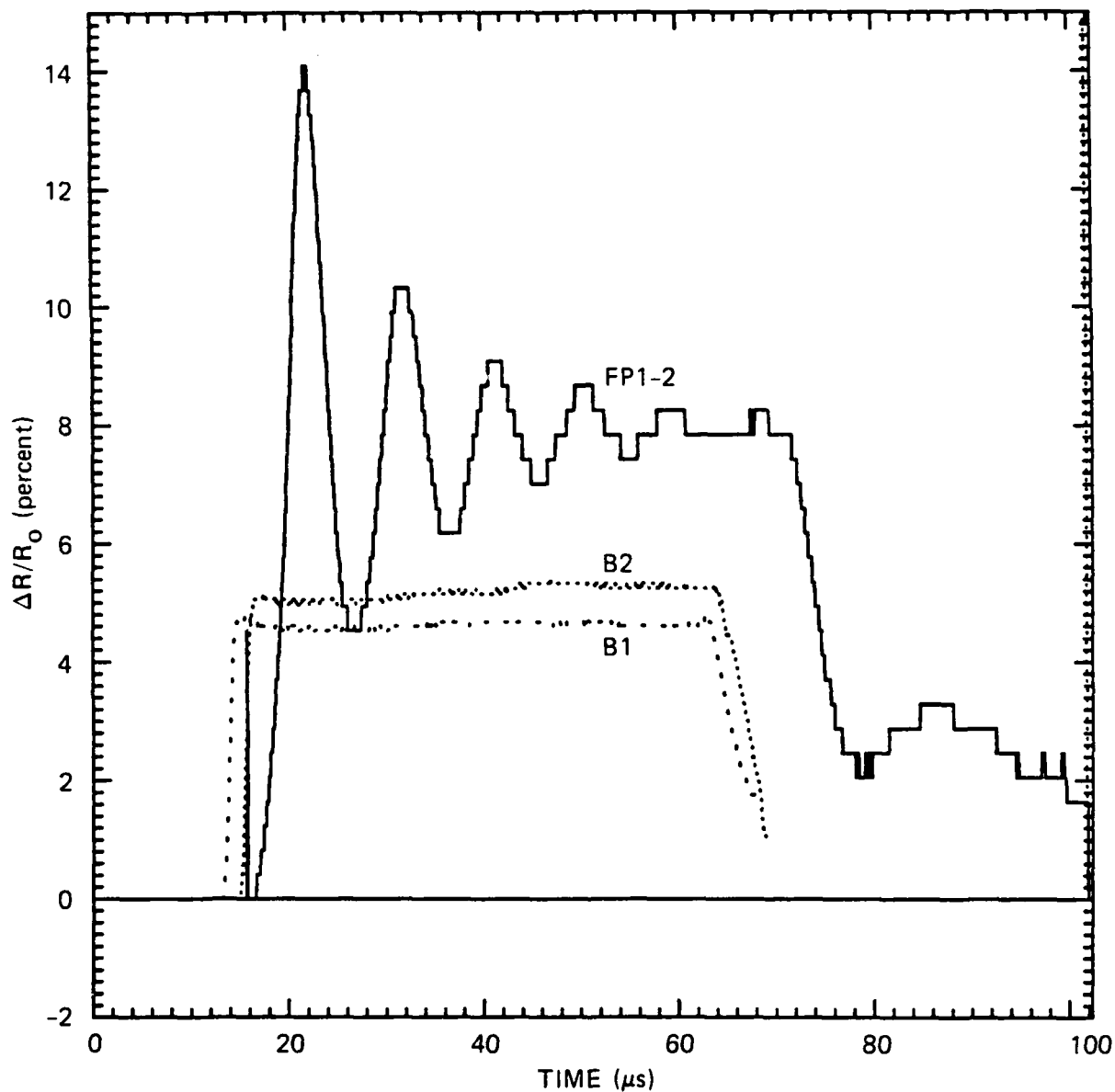
RA-2721-8

Figure 4.4. Relative resistance change records for flatpack stress gages in gage calibration experiment.



RA-2721-9

Figure 4.5. Comparison of relative resistance change records for flatpack stress gage and ytterbium element in Kapton/adhesive encapsulant.



RA-2721-10

Figure 4.6. Comparison of relative resistance change records for flatpack stress gage and ytterbium elements in Teflon/epoxy encapsulant.



mechanical state of the ytterbium element in a steel flatpack, and in the second simulation, we calculated the mechanical state of the ytterbium in a Kapton insulator. Using these mechanical states, we then calculated the relative change in resistance with Gupta's piezoresistance model. This model relates the relative change in resistance to the mechanical state of the ytterbium by the expression

$$\Delta R/R_0 = [\alpha(\Delta\sigma_1 + \Delta\sigma_2 + \Delta\sigma_3) + 2\beta\Delta\sigma_1 + \eta\Delta\varepsilon^P] + \Delta\varepsilon_1 - \Delta\varepsilon_2 - \Delta\varepsilon_3$$

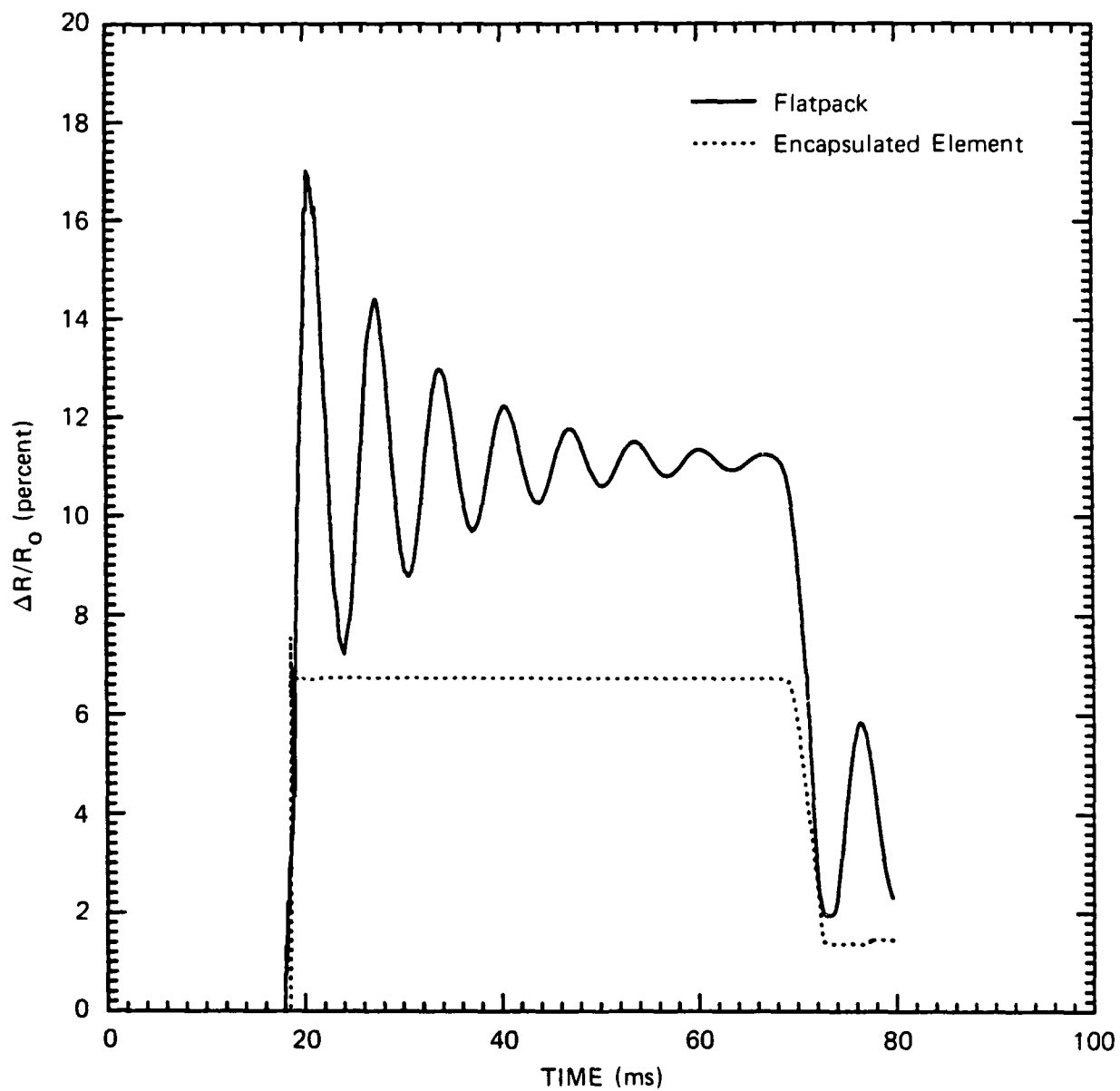
where  $\alpha$  and  $\beta$  are material-specific piezoresistance coefficients,  $\sigma$  and  $\varepsilon$  are the stress and strain states of the foil,  $\eta$  is a constant strain hardening coefficient, and  $\Delta\varepsilon^P$  is a measure of the accumulated plastic work. We measured the piezoresistance coefficients ( $\alpha$  and  $\beta$ ) in laboratory uniaxial stress "pull" tests following the procedure reported by Chen et al.,<sup>10</sup> but we did not measure  $\eta$ .

The relative resistance change calculated using the piezoresistance model for the flatpack and encapsulated gage are shown superposed in Figure 4.7. The main features observed in the experiment (Figures 4.5 and 4.6) are reproduced, namely, (1) oscillations about the equilibrium level for the flatpack and a square wave for the encapsulated gages and (2) a higher equilibrium ( $\Delta R/R_0$ ) level for the flatpack gage than for the encapsulated gage. Comparing this result with the experimental results shown in Figures 4.5 and 4.6, we find that the calculated equilibrium level for both the flatpack and encapsulated gages is about 30% to 40% higher than observed experimentally. We believe this difference may be due to the piezoresistance coefficients determined in the tension tests and used in the calculation, and although the overall mechanical response of the flatpack is accurately modeled, the specific material properties of the ytterbium need to be refined. In particular, we did not measure the ( $\eta$ ) term in equation (2), and this parameter is important for describing the contribution of the accumulation of plastic work to the resistance change.

#### 4.3.2 Transfer Function for Reducing Flatpack Data.

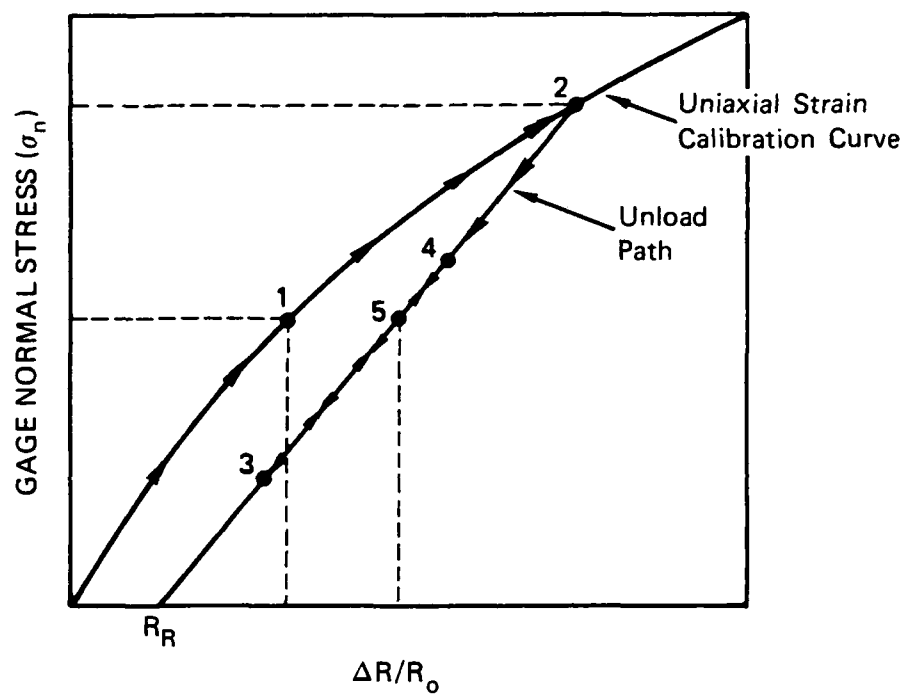
The current method of reducing flatpack data employs a transfer function approach relating the measured scalar, relative change in resistance, to the component of the stress tensor normal to the gage.

The data reduction procedure is described in Figure 4.8. This figure relates the normal stress applied to the gage to the relative change in resistance ( $\Delta R/R_0$ )



RA-2721-18

Figure 4.7. Calculated relative resistance change for flatpack and encapsulated ytterbium element using electromechanical piezoresistance (EP) model.



JA-8270-418

Figure 4.8. Empirical flatpack unfolding function for data reduction.

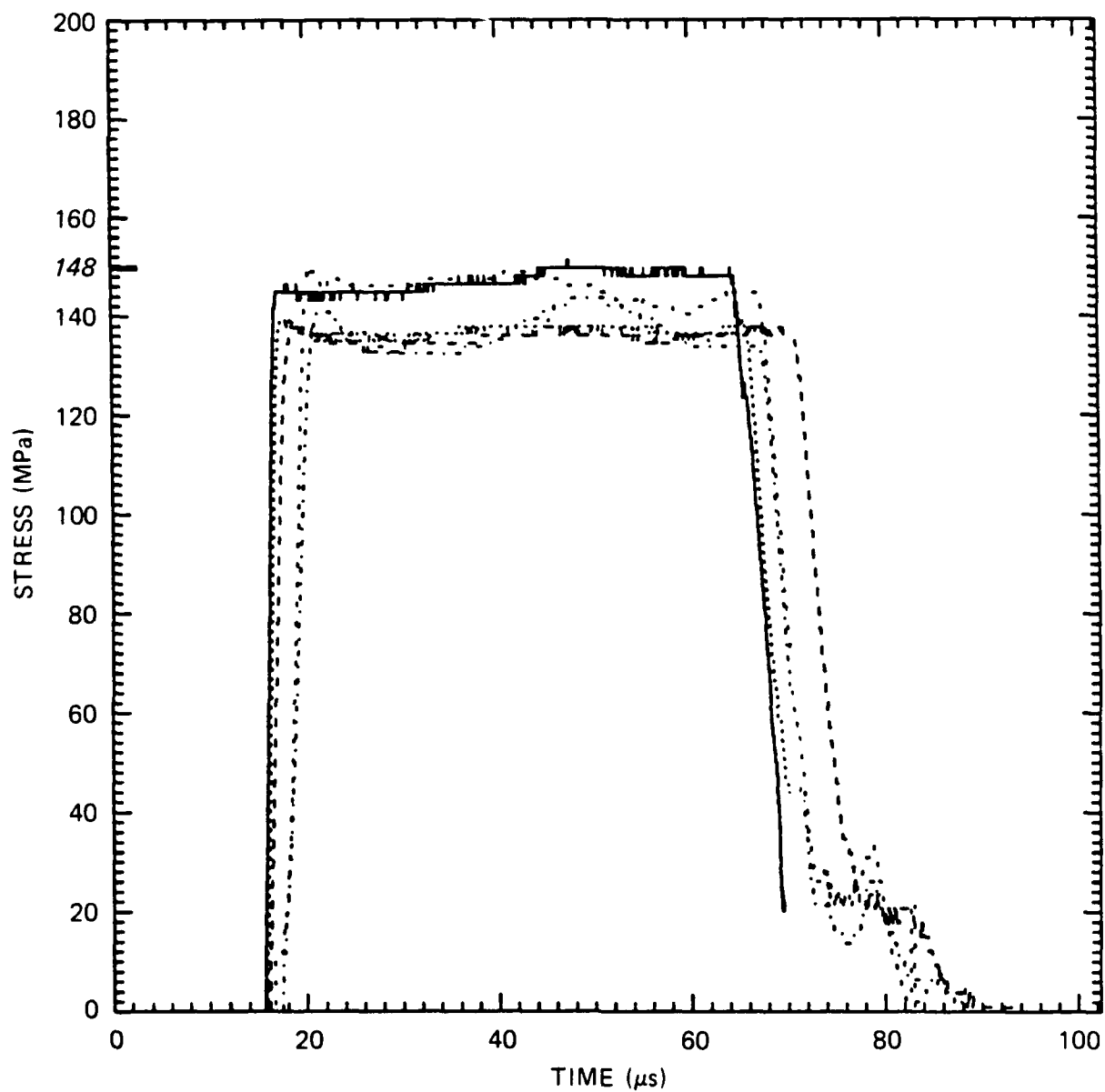
by the uniaxial strain calibration curve. This curve was developed from a series of uniaxial strain calibration experiments and is written as  $\sigma = e^A$  where

$$A = \left[ 2.38586 + 0.73608 \ln\left(\frac{\Delta R}{R_0}\right) - 0.057351 \ln\left(\frac{\Delta R}{R_0}\right)^2 \right. \\ \left. - 0.034949 \ln\left(\frac{\Delta R}{R_0}\right)^3 - 0.00379 \ln\left(\frac{\Delta R}{R_0}\right)^4 \right]$$

The calculated and observed differences in equilibrium ( $\Delta R/R_0$ ) levels between flatpacks and encapsulated elements can be explained by considering the different loading histories of the two cases and also the elastic-plastic behavior of ytterbium. In the first case, the encapsulated element is loaded to a point on the calibration curve (point 1 in Figure 4.8) where it remains in equilibrium with the free-field condition before unloading. In the second case, the flatpack initially loads to a much higher stress because of the different impedance of the flatpack and the matrix material (point 2). As the flatpack gage package equilibrates with the surrounding free-field, it goes through a series of load/unload/reload cycles (points 3 and 4), before it finally reaches an equilibrium state (point 5). The unload curve is below the loading curve because of plastic deformation of the ytterbium.

If we assume that the ytterbium unloading curve can be described by a linear and reversible path defined by the peak stress on the gage and the gage residual resistance, then we can reduce both encapsulated and flatpack ( $\Delta R/R_0$ ) data to stress. The current data reduction procedure is to use the calibration curve transfer function for loading to the measured peak relative change in resistance. After the peak, the unloading path is a line whose endpoints are defined as the peak change in resistance to the measured residual gage resistance.

We performed this data reduction procedure on the resistance change records for the encapsulated elements shown in Figure 4.3, and the results are shown superposed in Figure 4.9. All elements showed a peak stress within 10% of the known peak stress amplitude of 148 MPa. The data reduction procedure applied to the flatpack stress gages is shown in Figures 4.10 and 4.11, with the corresponding encapsulated elements of the same encapsulant and mounting process shown superposed. Although the relative resistance change records showed vastly different behavior and equilibrium levels, we observe excellent agreement for both the flatpack and encapsulated gages between the measured and known free-field stress using the current data reduction procedure.



RA-2721-11

Figure 4.9. Composite stress histories reduced from  $\Delta R/R_0$  records for encapsulated elements (B1-B5) in gage calibration experiment.

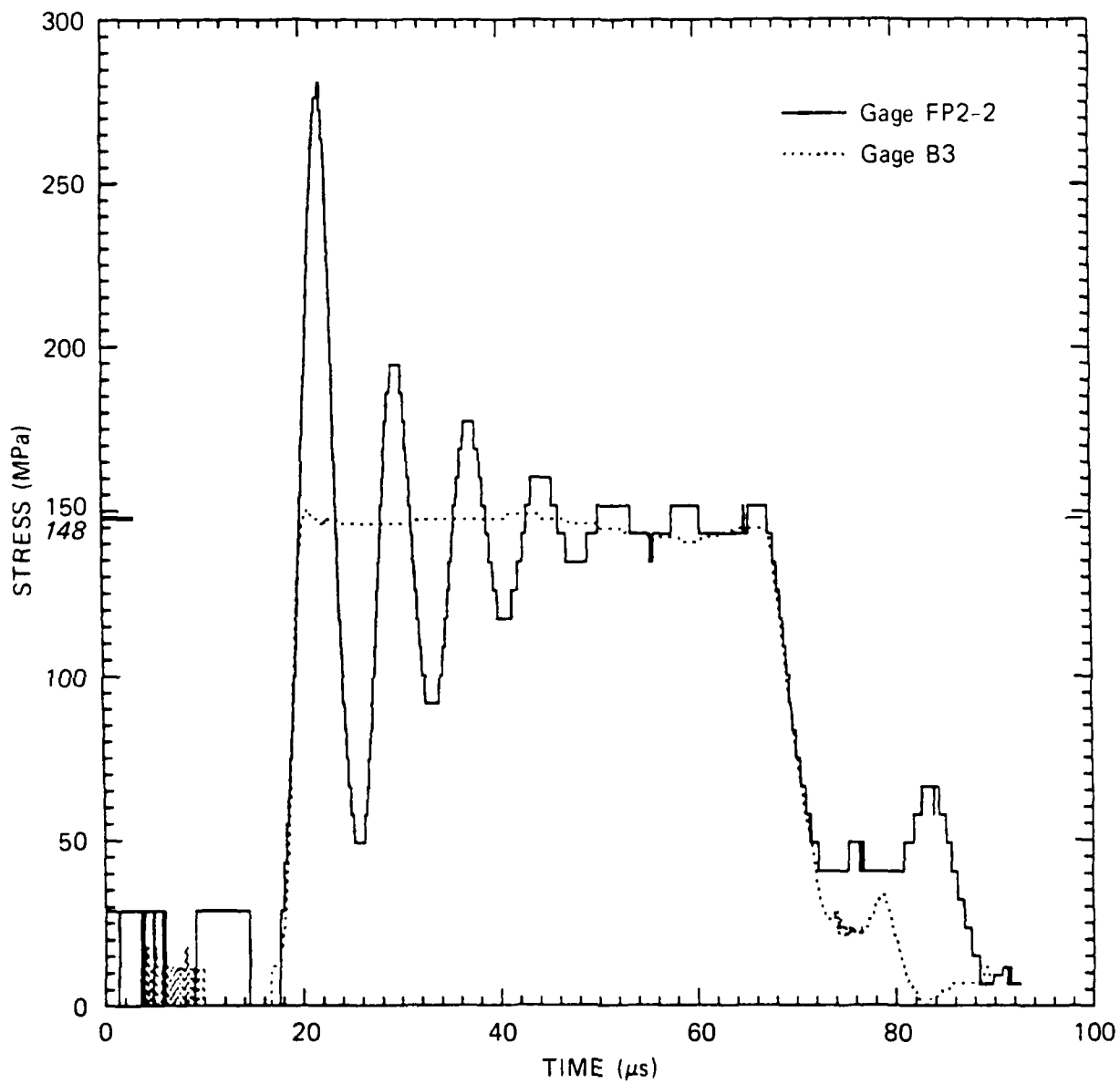


Figure 4.10. Comparison of stress history reduced from relative resistance change record for photo-etched ytterbium element in Kapton/adhesive encapsulant.

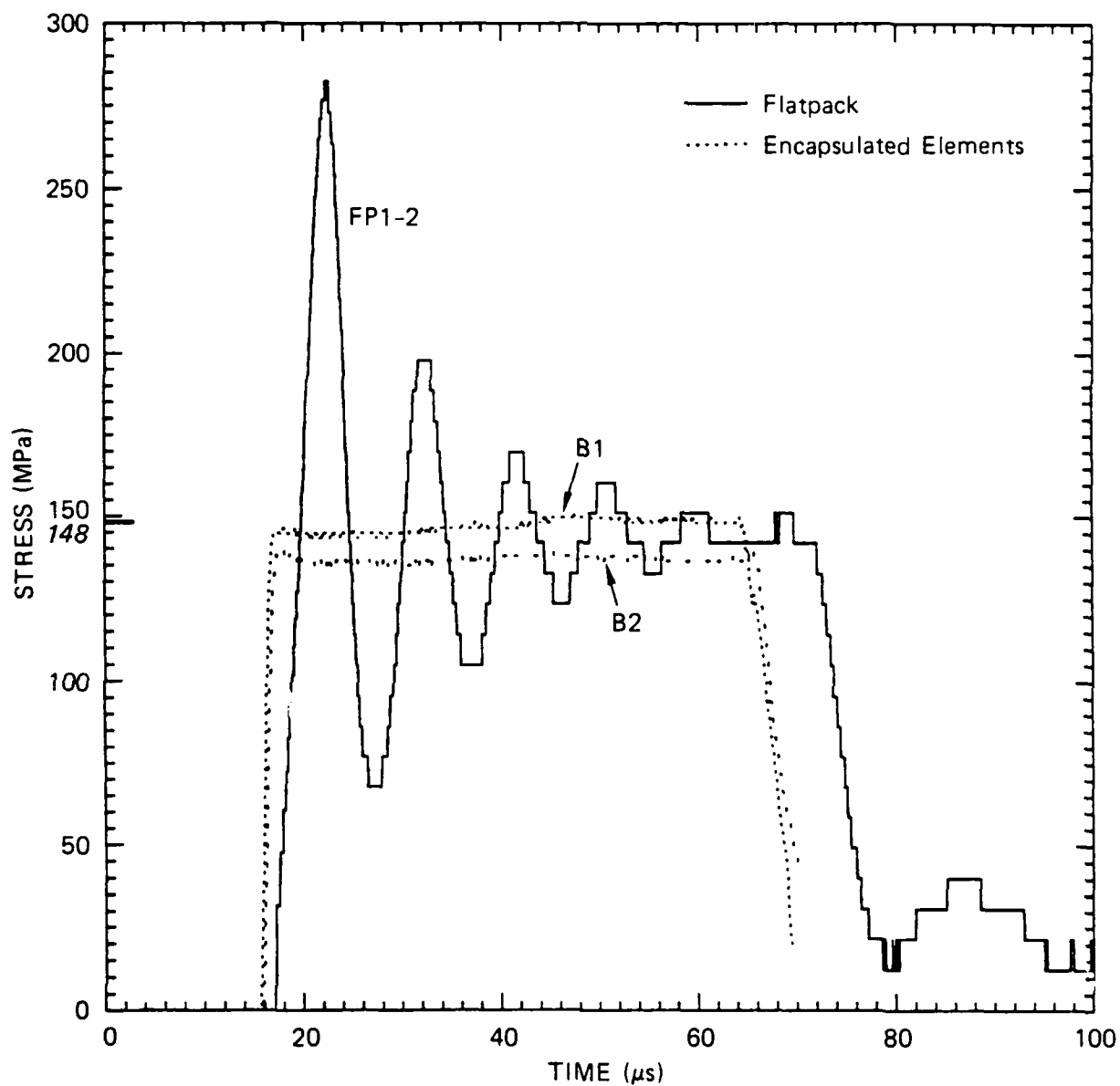
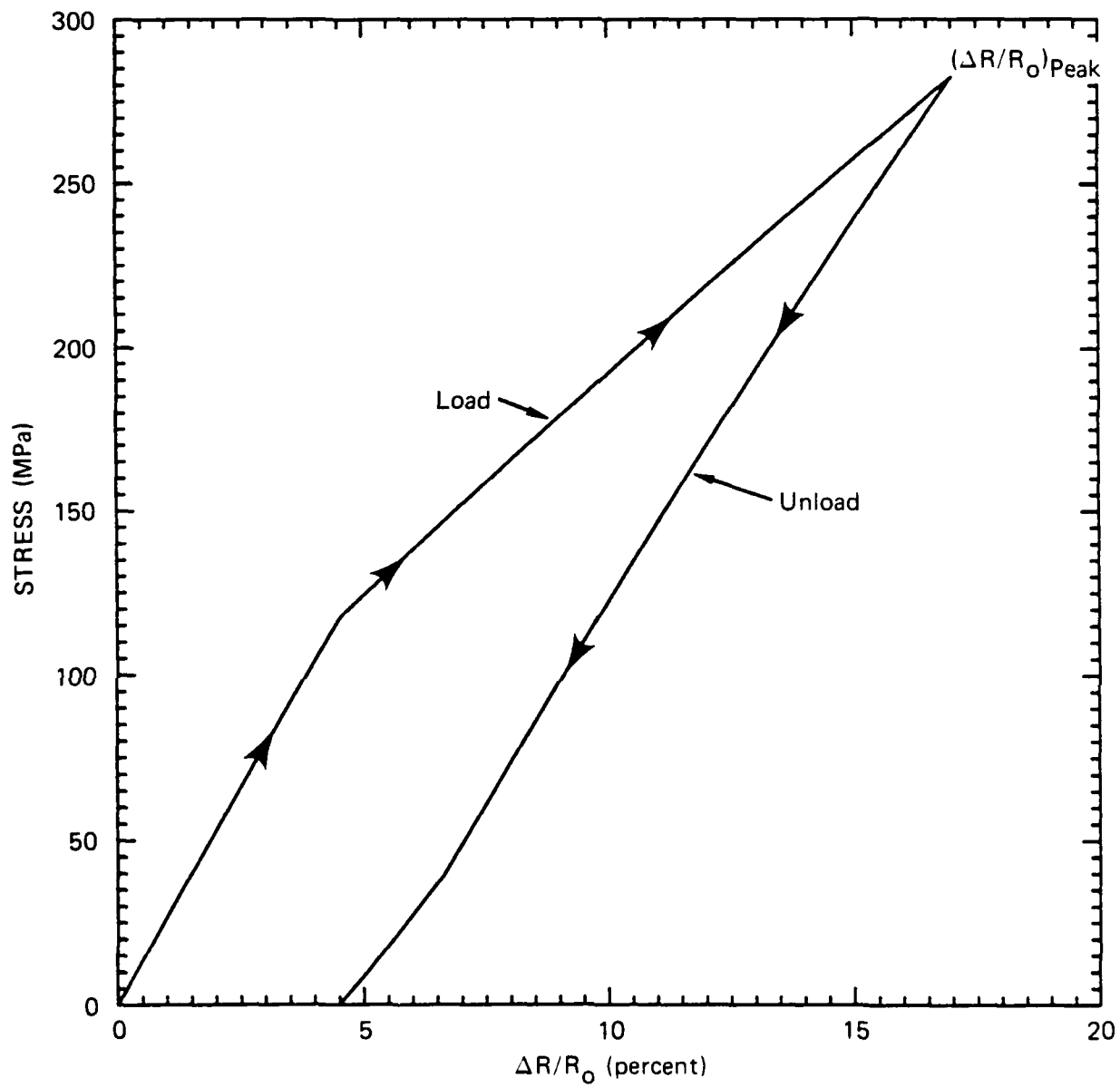


Figure 4.11. Comparison of stress histories reduced from relative resistance change records for flatpack stress gage and ytterbium elements in Teflon/epoxy encapsulant.

The data reduction procedure is supported by the results of the  $(\sigma - \Delta R/R_0)$  relationship calculated using the flatpack response model shown in Figure 4.12. The calculation also shows a linear/reversible path during the equilibration of the flatpack with the free-field. This unloading path is defined by the peak  $(\Delta R/R_0)$  of the record and the gage residual resistance.





RA-2721-19

Figure 4.12. Calculated load/unload path of ytterbium element inside a flatpack using flatpack response model.

## SECTION 5

### RECOMMENDATIONS FOR FUTURE WORK

The approach to gage validation described in this report and applied to rained sand test beds should be applied to other materials of interest (e.g., wet sand, hard rock). Specifically, the MIPV gage needs to be validated in each material before use as a Lagrangian gage in other uniaxial strain environments to calculate the free-field stress history.

Because the gage validation approach is restricted to uniaxial flow conditions, the flyer plate diameter of the AFWL facility should be increased (for test beds where the release wave velocity is significantly higher than the shock velocity) to extend the time before arrival of two-dimensional effects at the measurement locations. Secondly, the time of arrival and magnitude of the edge effects should be measured in subsequent experiments.

In terms of the flatpack response model, we recommend (1) high resolution two-dimensional calculations of flatpack response to more accurately determine the mechanical state of the ytterbium element and (2) continued testing of the ytterbium foil to refine the piezoresistance coefficients for the EP model.

## SECTION 6

### REFERENCES

1. D. E. Grady, C. W. Smith, G. M. Muller, K. D. Mahrer, and C.F. Peterson, "In Situ Constitutive Relations of Soils and Rocks," Interim Report DNA 36712, Contract DNA 001-73-C-0124, Stanford Research Institute, Menlo Park, CA (March 1974).
2. P. S. DeCarli et al., "Stress-Gage System for the Megabar (100 GPa) Range," Draft Final Report, Contract DNA 001-75-C-0029, Stanford Research Institute, Menlo Park, CA (June 1976).
3. D. D. Keough et al., "Research on Advanced Silo Hardening (ASH) Instrumentation and Material Properties," Final Report, Contract DNA 001-85-C-0085, SRI International, Menlo Park, CA (in progress).
4. L. Seaman, "Lagrangian Analysis for Multiple Stress or Velocity Gages in Attenuating Waves," J. Appl. Phys. 45, 4303-4314 (1974).
5. E. Rinehart, "Gage Validation Using a 2.4-m-diameter Flyer Plate," Draft Report CRTA-TR-3750-2, AFWL Contract F29601-85-C-0004 (July 1987).
6. C. E. Anderson, P.E. O'Donoghue, J.D. Renick, D.K. O'Kelly, and C. Felice, "Flyer Plate Impact of Dry Soils: An Instrumentation Calibration Technique," Paper presented at DNA Conference on Instrumentation For Nuclear Weapons Effects Testing, Arlington, VA (October 6-8, 1987).
7. C. Felice, "The Response of Soils to Impulse Loads Using a Split-Hopkinson Pressure Bar Technique," AFWL-TR-85-92, Kirtland AFB, NM (May 1986).
8. I. C. Skidmore, Appl. Mater. Res. 1 131 (1965).
9. Y. M. Gupta, "Stress Measurements Using Piezoresistance Gauges: Modeling the Gauge as an Elastic-Plastic Inclusion," J. Appl. Phys. 54(11), 6256-6266 (November 1983).
10. D. Y. Chen, Y. M. Gupta, and M. H. Miles, "Quasistatic Experiments to Determine Material Constants for the Piezoresistance Foils Used in Shock Wave Experiments," J. Appl. Phys. 55(11), 3984-3993 (June 1984).